

Received 15 August 2022, accepted 5 September 2022, date of publication 12 September 2022,  
date of current version 22 September 2022.

Digital Object Identifier 10.1109/ACCESS.2022.3206025

## RESEARCH ARTICLE

# Intrusion Detection System for Multilayer-Controlled Power Electronics-Dominated Grid

AHMAD KHAN<sup>1</sup>, (Student Member, IEEE),  
MOHAMMAD B. SHADMAND<sup>1</sup>, (Senior Member, IEEE),  
AND SUDIP K. MAZUMDER<sup>1</sup>, (Fellow, IEEE)

Department of Electrical and Computer Engineering, University of Illinois at Chicago, Chicago, IL 60607, USA

Corresponding author: Mohammad B. Shadmand (shadmand@uic.edu)

**ABSTRACT** This article presents an intrusion detection system (IDS) for a multi-layer-controlled power electronics-dominated grid (PEDG). This IDS improves the situational awareness of PEDG against malicious set-points from a compromised upper control layer. Firstly, a mathematical theory is developed for deriving a safe operation region. This mathematical theory extends the stability margins inferred from  $P-V$  curves to the abstract concept of morphisms. Particularly, there are two morphisms for each point of common coupling (PCC) bus when operating in the safe operation region: (*Morphism 1*) PCC bus voltage mapped to network set-points, and (*Morphism 2*) network set-points mapped to PCC bus voltage. *Morphism 1* is used for anomaly detection. Explicitly, observation of a non-zero imaginary-part in the PCC voltage  $L_2$  norm is evidence of an anomaly. *Morphism 2* is utilized for independent decision making at the primary layer of the dispersed energy generator (DEG) during intrusion scenarios. *Morphism 2* is an alternative for the secondary layer when the dispatched set-points are not trusted. The theoretical analysis is verified by several case studies to substantiate the situational awareness against malicious set-points and consequently enhancing the cybersecurity aspects of the PEDG.

**INDEX TERMS** Power electronics-dominated grid, safe operation region, intrusion detection system, situational awareness.

## LIST OF SYMBOL

$t$  Time.  
 $\tau$  Dummy intermediate variable for integrals.  
 $C_{DCi}$  DC-link capacitor of the  $i^{th}$  grid-feeding inverter.  
 $L_i$  Filter inductor of the  $i^{th}$  grid-feeding inverter.  
 $R_i$  Filter inductor resistance of the  $i^{th}$  grid-feeding inverter.  
 $\omega$  Nominal angular frequency of the network.  
 $P_i$  Active power of the  $i^{th}$  grid-feeding inverter.  
 $P_{Li}$  Active power of the  $i^{th}$  grid-feeding inverter load.  
 $P_{PCCi}$  Active power of the  $i^{th}$  local PCC bus.  
 $Q_i$  Reactive power of the  $i^{th}$  grid-feeding inverter.

$Q_{Li}$  Reactive power of the  $i^{th}$  grid-feeding inverter load.  
 $Q_{PCCi}$  Reactive power of the  $i^{th}$  local PCC bus.  
 $S_{Rated}$  Rated appeared power of the  $i^{th}$  grid-feeding inverter.  
 $f_{sw}$  Switching frequency of the  $i^{th}$  grid-feeding inverter.  
 $P_{Refi}$  Active power reference of the  $i^{th}$  grid-feeding inverter.  
 $Q_{Refi}$  Reactive power reference of the  $i^{th}$  grid-feeding inverter.  
 $Z_{ij}$  Line impedance between PCC bus  $i$  and  $j$ .  
 $R_{ij}$  Line resistance between PCC bus  $i$  and  $j$ .  
 $L_{ij}$  Line inductance between PCC bus  $i$  and  $j$ .  
 $j$  Square root of  $-1$ .  
 $\mathbb{R}$  Real number set symbol.  
 $\mathbb{C}$  Complex number set symbol.  
 $N$  Number of DEGs.

The associate editor coordinating the review of this manuscript and approving it for publication was Peter Palensky<sup>1</sup>.

$\ X\ _2$	$L_2$ norm of $X$ .	$B_i$	Imaginary part of the $i^{th}$ local PCC bus phasor voltage.
$X^*$	Complex conjugate of $X$ .	$R_{Thi}$	Thevenin resistance seen at the $i^{th}$ local PCC bus.
$X^T$	Transposition of $X$ .	$L_{Thi}$	Thevenin inductance seen at the $i^{th}$ local PCC bus.
$\vec{X}$	Phasor quantity of $X$ .	$f$	Developed Morphism 1: Generalization of the inverse of the P-V curve.
$\text{Re}\{X\}$	Real part of $X$ .	$g$	Developed Morphism 2: Generalization of the P-V curve.
$\text{Im}\{X\}$	Imaginary part of $X$ .	$h$	Ohm's law across linear resistor ( $R$ ) as a morphism mapping current ( $i_R$ ) into voltage ( $v_R$ ).
$u_{Pi}$	LTI MIMO open loop state space active power dynamics input.	$w$	Ohm's law across linear resistor ( $R$ ) as a morphism mapping voltage ( $v_R$ ) into current ( $i_R$ ).
$u_{Qi}$	LTI MIMO open loop state space reactive power dynamics input.	$A_{CLi}$	Closed loop control of the $i^{th}$ grid-feeding inverter state matrix.
$v_{DCi}$	DC link voltage of the $i^{th}$ grid-feeding inverter.	$x_{CLi}$	Closed loop control of the $i^{th}$ grid-feeding inverter states vector.
$v_{PCCi}$	$i^{th}$ local PCC voltage.	$P_{CLi}$	Closed loop control of the $i^{th}$ grid-feeding inverter linear quadratic Lyapunov stability theorem P matrix.
$v_{PCCi}^\alpha$	Alpha component of the $i^{th}$ local PCC voltage.	$Q_{CLi}$	Closed loop control of the $i^{th}$ grid-feeding inverter linear quadratic Lyapunov stability theorem Q matrix.
$v_{PCCi}^\beta$	Beta component of the $i^{th}$ local PCC voltage.	$V_{CLi}(x_{CLi})$	Lyapunov function of the $i^{th}$ grid-feeding inverter closed loop control.
$i_{PCCi}$	$i^{th}$ local PCC current.		
$i_{PCCi}^\alpha$	Alpha component of the $i^{th}$ local PCC current.		
$i_{PCCi}^\beta$	Beta component of the $i^{th}$ local PCC current.		
$m_i$	$i^{th}$ grid-feeding inverter modulation index.		
$m_i^\alpha$	Alpha component of the $i^{th}$ grid-feeding inverter modulation index.		
$m_i^\beta$	Beta component of the $i^{th}$ grid-feeding inverter modulation index.		
$\Omega_{SOR_i}$	Projection function for safe operation region of the $i^{th}$ local PCC bus.		
$\Omega_{SNOR_i}$	Projection function for stable/normal operation region of the $i^{th}$ local PCC bus.		
$e_{Pi}$	Error on active power of the $i^{th}$ grid-feeding inverter.		
$e_{Qi}$	Error on reactive power of the $i^{th}$ grid-feeding inverter.		
$v_{Pi}$	Active power control output of the $i^{th}$ grid-feeding inverter.		
$v_{Qi}$	Reactive power control output of the $i^{th}$ grid-feeding inverter.		
$K_{Ppi}$	Active power control proportional gain of the $i^{th}$ grid-feeding inverter.		
$K_{Qpi}$	Reactive power control proportional gain of the $i^{th}$ grid-feeding inverter.		
$K_{Pii}$	Active power control integral gain of the $i^{th}$ grid-feeding inverter.		
$K_{Qii}$	Reactive power control integral gain of the $i^{th}$ grid-feeding inverter.		
$\vec{v}_{Thi}$	Thevenin voltage phasor seen at the $i^{th}$ local PCC bus.		
$\delta_{Thi}$	Thevenin voltage angle seen at the $i^{th}$ local PCC bus.		
$\delta_{PCCi}$	$i^{th}$ local PCC bus voltage phasor angle.		
$V_g$	Grid voltage peak.		
$A_i$	Real part of the $i^{th}$ local PCC bus phasor voltage.		

## I. INTRODUCTION

The futuristic energy paradigm implicates high penetration of nonsynchronous generation at the grid edge through embracing dispersed energy generators (DEGs) [1], [2]. At the grid edge, grid-feeding inverters are projected to be the prevailing type of DEGs. In this mode of operation, the DEGs are following the inertial response of the network and their capabilities are confined in injecting/absorbing current into/from their local point of common coupling (PCC) without considering upstream network constraints and requirements [3]. Accordingly, these DEGs are typically unobservable to the upstream network and vice versa. Henceforth, real-time system level coordination and management is crucial to ensure the optimal utilization of unobservable DEGs that are installed behind the meters and offer an additive situational awareness to the system [4], [5].

The multi-layer-controlled power electronics-dominated grid (PEDG) is demonstrating to be an effective example that is enabling DEGs to achieve the U.S. Department of Energy's 100% nonsynchronous generation based U.S. power grid [6]. The PEDG is a cluster of distinct scale DEGs that can be aggregated into a single coherent entity. The multi-layer-controlled PEDG is able to function as an intermediate interface between transmission and distribution system operators [7]. Consequently, offering

superior observability and controllability on DEGs and permits optimal utilization of inverters-based resources features. Various multi-layer controlled PEDG deployments exist around the world such as the ones reported in documents in [8] and [9].

The futuristic 100% nonsynchronous generation-based power grid targeted in 2050 by the U.S. Department of Energy is anticipated to be vulnerable to malicious cyber-attacks. This is because of the more dispersed generation that will operate outside the realm of old-fashioned power-plant administrative domain through employing more DEGs at the grid edge [10], [11], [12], [13], [14]. The attack might be introduced into the PEDG infrastructure through the communication medium that enables its harmonious operation. Security breach in the cyber-layer of a PEDG has a direct influence on its physical layer, which disrupts its nominal operation. A severe stealthy cyber-attack typically spreads throughout the grid steadily compromising the cyber layer. This makes the detection of such a stealthy attack extremely challenging at early stages using conventional protection and intrusion detection schemes [15], [14], [16].

This article is enhancing the situational awareness against malicious PQ set-points requests from a compromised secondary and cyber layer. These malicious set-points are assigned by a stealthy intruder breaching undetectably into the secondary control and cyber layer of the PEDG depicted in Fig. 1. Furthermore, this situational awareness improvement impacts positively the cybersecurity of the PEDG. In fact, according [17], situational awareness feature offers a direct improvement of the system cyber-security aspects. As situational awareness does not only provide accurate observation, but also ensures availability of necessary functions that support predicting operation projections and identifying potential risks [18]. Moreover, a mathematical theory is developed for deriving a safe operation region (SOR). This mathematical theory extends the stability margins inferred from  $P - V$  curves to the abstract concept of morphisms (see Appendix C for Morphism theoretical background). Particularly, there are two morphisms for each PCC bus when operating in the SOR: (*Morphism 1*) PCC bus voltage mapped to network set-points that is structured as  $\mathbb{R}$  to  $\mathbb{R}^{2N}$  mapping, and (*Morphism 2*) network set-points mapped to the PCC bus voltage that is structured as  $\mathbb{R}^{2N}$  to  $\mathbb{R}$  mapping. Where  $N$  is the number of PCC buses. *Morphism 1* is used for anomaly detection originating from the secondary layer dispatched set-points manipulation. Explicitly, observation of a non-zero imaginary-part in the PCC voltage  $L_2$  norm is evidence of an anomaly. Note that,  $L_2$  norm properties are: nonnegativity, definiteness, triangle inequality, and homogeneity must be satisfied in SOR for PCC voltage as this preserves the  $\mathbb{R}$  to  $\mathbb{R}^{2N}$  mapping structure. Inspecting an imaginary-part invalidates nonnegativity property of the PCC voltage  $L_2$  norm (i.e.,  $\mathbb{R}$  to  $\mathbb{R}^{2N}$  is not preserved see Appendix D for theoretical proof). *Morphism 2* is utilized for independent decision making at the primary layer of the DEG during cyber intrusion scenarios. In other words, *Morphism 2* is an alternative for

the secondary layer when the dispatched set-points are not trusted.

In the literature, the capability of synchronous generator is estimated through the concept of capability chart. This chart provides the range of dispatchable PQ set-points without jeopardizing the stability of the synchronous generator [19]. The notion of capability chart was first time utilized for multi-layer-controlled renewable based grid in [20]. This capability chart was used as conventional generators capability charts that are employed in scheduling and dispatching optimization. In other words, set-points that belong to the capability chart are guaranteed to be executable when requested by the upstream network. Though, the capability charts for renewable based grids are more complex compared to conventional generators. This is because renewable based grid capability charts are representing aggregation of various DEGs. An example of such capability charts is used to estimate the reactive power injection capability at different active power levels in [21]. Another work is suggesting a methodology for approximating capability chart numerically using repeated time domain simulations in [22]. In general, the capability chart is obtained by repeated load flow solutions for various scenarios that often are selected randomly. After that, the realistic load flow solutions consequence to points that are constructing the capability chart. Another approaches that are reported in the literature for approximating the capability charts are employing geometrical hypothesis such as polyhedron, ellipse, and so on [23]. Furthermore, capability charts estimation with incorporation of randomness is reported in [24]. Yet, these methods extensively rely on repetitive load flow solutions that needs to be executed in secondary or tertiary layers, which even turns out to be challenging to utilize fast load flow algorithms due to the dominate resistive nature for the distribution network [25]. Furthermore, the considered potential attack model, in which the intruder is compromising the secondary layer controller and existing load flow algorithms, mandates another sanity checkpoint at the primary layer for realizing an effective intrusion detection. Hence, to our knowledge, utilizing the existing capability charts for intrusion detection against operational PQ set-points manipulation is not viable from the perspective of the primary layer. The contributions of this paper are summarized in the following bullet points:

- A mathematical theory extends the stability margins inferred from  $P - V$  curves to the abstract concept of morphism. This morphism simplifies understanding the operation limits of the unobservable DEGs without relying on repeated load flow solution at secondary/tertiary control layers, thus creating an independent framework for decisions making at the primary layer.
- Intrusion detection by utilizing the SOR as a sanity checkpoint for PQ set-points assignments by potentially compromised secondary layer; thus, detecting and preventing a cyber intruder that is requesting malicious set-points from the DEGs.

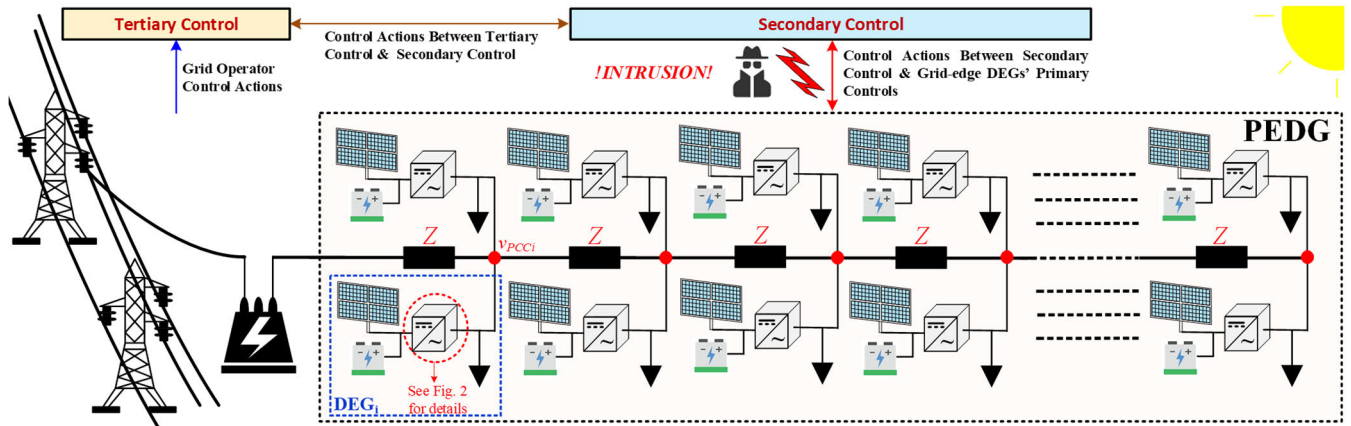


FIGURE 1. Multi-layered controlled PEDG concept extended to the grid edge with unobservable single-phase DEGs in grid-feeding mode of operation.

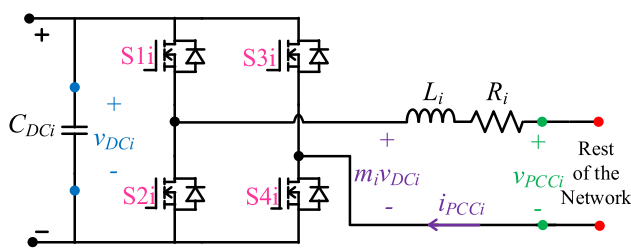


FIGURE 2. Grid-feeding primary control layer considered for DEGs in the PEDG: inverter structure.

The remainder of the article is structured as follows: Section II is the illustration of the multi-layer controlled PEDG considered in this article. Section III is mathematical theory of deriving the SOR which construct the *Morphism 2*. Section IV summarizes steps to utilize the *Morphism 1* and *Morphism 2* for intrusion detection. Section V discusses the results. Finally, section VI concludes the article.

## II. MULTI-LAYER CONTROLLED PEDG NETWORK UNDERSTUDY

The multi-layer controlled PEDG network understudy is portrayed in Fig.1. In this PEDG, the main PCC bus voltage is the potential difference between the low side positive terminal of the distribution pole transformer and the ground conductor (see  $v_{PCC1}$  in Fig. 1). Similarly, the internal local PCC buses are considered as each node that consumers at the grid edge are feeding their local loads (see  $v_{PCC2}, v_{PCC3}, \dots, v_{PCCn}$  in Fig. 1). In addition, DEGs are installed at internal local PCC buses. The grid-feeding inverter in Fig. 2 primary control layer considered in this work for DEGs is depicted in Fig. 3. The open loop system is represented by the multiple input multiple output (MIMO) linear time invariant (LTI) state space in (1).

$$\begin{bmatrix} \frac{dP_i}{dt} \\ \frac{dQ_i}{dt} \end{bmatrix} = \begin{bmatrix} -R_i L_i^{-1} & -\omega \\ \omega & -R_i L_i^{-1} \end{bmatrix} \begin{bmatrix} P_i \\ Q_i \end{bmatrix}$$

$$\begin{aligned} & + \begin{bmatrix} 0.5L_i^{-1} & 0 \\ 0 & 0.5L_i^{-1} \end{bmatrix} \begin{bmatrix} u_{Pi} \\ u_{Qi} \end{bmatrix} \\ u_{Pi} &= m_i^\alpha v_{DCi} v_{PCCi}^\alpha + m_i^\beta v_{DCi} v_{PCCi}^\beta - \|\vec{v}_{PCCi}\|_2^2 \\ u_{Qi} &= m_i^\alpha v_{DCi} v_{PCCi}^\beta - m_i^\beta v_{DCi} v_{PCCi}^\alpha \\ \|\vec{v}_{PCCi}\|_2 &= \sqrt{v_{PCCi}^{\alpha 2} + v_{PCCi}^{\beta 2}} \\ e_{Pi} &= P_{Refi} - P_i \\ v_{Pi} &= e_{Pi} K_{Ppi} + K_{Pii} \int e_{Pi}(\tau) d\tau \\ e_{Qi} &= Q_{Refi} - Q_i \\ v_{Qi} &= e_{Qi} K_{Qpi} + K_{Qii} \int e_{Qi}(\tau) d\tau \\ \frac{d^2 e_{Pi}}{dt^2} &= -\left(K_{Ppi} + R_i L_i^{-1}\right) \frac{de_{Pi}}{dt} - K_{Pii} e_{Pi} \\ \frac{d^2 e_{Qi}}{dt^2} &= -\left(K_{Qpi} + R_i L_i^{-1}\right) \frac{de_{Qi}}{dt} - K_{Qii} e_{Qi} \end{aligned} \quad (1)$$

This control is guaranteeing that primary control layer stability. The proof for the stability of the primary control layer equilibrium is detailed in Appendix A with linear quadratic Lyapunov stability theorem. Similarly, Appendix B details potential instabilities that might originate from a cyber-attacker at the secondary control layer manipulating the dispatched PQ set-points.

## III. SAFE OPERATION REGION DERIVATIONS AND INTURSION SCENARIO

### A. INTRUSION AND MALICIOUS PQ SET-POINTS IMPACT

Consider the exemplification in Fig. 4 of the multi-layer controlled PEDG understudy shown in Fig. 1, if a stealthy cyber intruder took control over the cyber layer and he is targeting the  $i^{th}$  local PCC bus in Fig. 4 by manipulating the operation PQ set-points that are passing from the secondary layer to the primary layer of the DEG. From the stealthy intruder perspective, he is altering the operation set-points and observing the local measurement to understand the impact of his set-points manipulation. The intruder could initiate catastrophic effect by pushing the targeted PCC bus to operate outside its stable

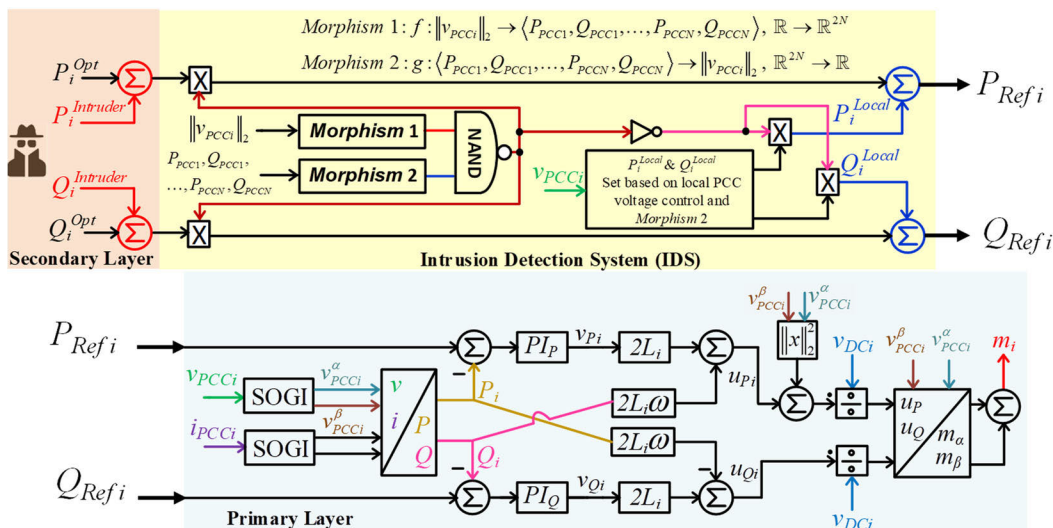


FIGURE 3. Grid-feeding primary control layer considered for DEGs in the PEDG: controller structure with measurements, nonlinear coordinate the transformation illustration, and the intrusion detection system.

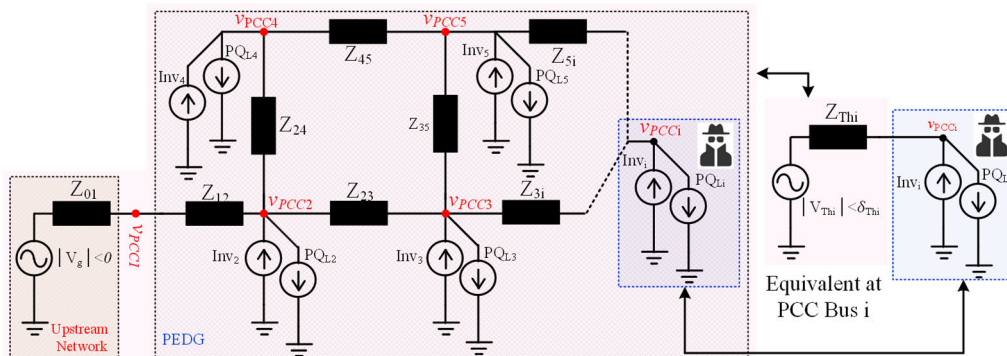


FIGURE 4. General PEDG network, illustrating the  $i^{th}$  local PCC terminals equivalent circuit.

set-points domain by slowly and randomly changing the PQ set-points [14]. Therefore, the hypothesis in this article is that the primary layer will be equipped with the SOR, as a sub-layer in primary. Then, if the DEG is pushed to operate outside SOR by the secondary layer manipulated PQ set-points, the primary layer considers that the set-points passing from the secondary layer are compromised. Moreover, the methodology that is optimal to understand an intrusion occurred or not is by witnessing if the PQ dispatched set-points passing to primary control layer from the upper control layer are intended to induce an instability. Since rationally, the upper control must solve optimization on network level and thus the stability of the network is one of the crucial constrains in that optimization. Hence, to catch that there is stealthy intruder from the limited primary layer perspective, witnessing requests of PQ set-points that belongs to unstable operation region (UOR) is helpful in detection. The method applied does not depend on measurements for deciding intrusion occurred or not. The process of intrusion detection is

initiated by checking the structural preservation of the *Morphism 1* which is a sort of abstraction of the inverse of the generalized P-V curve (2).

$$f : \|\vec{v}_{PCCi}\|_2 \rightarrow \langle P_{PCC1}, Q_{PCC1}, \dots, P_{PCCN}, Q_{PCCN} \rangle, \mathbb{R} \rightarrow \mathbb{R}^{2N} \quad (2)$$

The structure preservation is not sustained when *Morphism 1* is producing a non-zero imaginary valued  $L_2$  norm. Then, the decision that this anomaly is due to an intrusion or not is based on authenticating the set-point passing for upper layer into *Morphism 2* (i.e., the generalized PV curve expressed in (3)).

$$g : \langle P_{PCC1}, Q_{PCC1}, \dots, P_{PCCN}, Q_{PCCN} \rangle \rightarrow \|\vec{v}_{PCCi}\|_2, \mathbb{R}^{2N} \rightarrow \mathbb{R} \quad (3)$$

If the structure of *Morphism 2* is not preserved i.e., non-zero imaginary valued  $L_2$  in *Morphism 2*, then definitely the upper network set-point are compromised. Furthermore, Fig. 3 shows the details of the intrusion detection system.

Specifically, the *Morphism 1* and *Morphism 2* in Fig. 3 produce a binary output 1 when their structure preservation are not sustained (i.e., both  $L_2$  norms produce a non-zero imaginary part). Otherwise, the *Morphism 1* and *Morphism 2* produce binary output 0. Then, these two signals pass through a NAND gate to ignore or consider the upper layer set-point request. If intrusion happened the DEGs operate in alternative control scheme that corrects the local PCC voltage terminal using *Morphism 2*. Additionally, see Appendix C for *Morphism* background. Appendix D proves having a none-zero imaginary part in the  $L_2$  norm means that the set-points belong to UOR and structural preservation of *Morphism 2* is no sustained.

**B. SAFE OPERATION REGION “i.e., MORPHISM 2”**

To understand how the PEDG stability is impacted by grid-feeding inverters’ set-points variations; in this subsection, an illustration of how a single grid-feeding inverter (i.e., representing an unobservable DEG at the grid edge) impacts its local PCC voltage in a general single-phase network is carried out. In this situation, the network is reduced to two buses where the  $i^{th}$  targeted grid-feeding inverter sees the rest of the network from its local PCC terminals as a large synchronous impedance in series connection with a Thevenin voltage source (see Fig. 4). This Thevenin voltage source ( $\vec{v}_{Thi}$ ) is embedding the rest of the network PQ set-points. Then, the relation between the Thevenin voltage ( $\vec{v}_{Thi}$ ) and the local PCC voltage for the  $i^{th}$  grid-feeding inverter ( $\vec{v}_{PCCi}$ ) is given by,

$$\vec{v}_{PCCi} = (R_{Thi} + j\omega L_{Thi}) \vec{i}_{PCCi} + \vec{v}_{Thi} \quad (4)$$

where  $R_{Thi}$  is the Thevenin resistance seen by the  $i^{th}$  grid-feeding inverter from its local PCC terminals to the main PCC bus terminal,  $L_{Thi}$  is the Thevenin inductance seen by the  $i^{th}$  grid-feeding inverter from its local PCC terminals to the main PCC bus terminals,  $\omega$  is the nominal angular frequency of the network, and  $\vec{i}_{PCCi}$  is the current injected by the  $i^{th}$  grid-feeding inverter into its local PCC terminals. Furthermore, in equation (2) the local PCC voltage is as (5).

$$\vec{v}_{PCCi} = \|V_{PCCi}\|_2 \angle \delta_{PCCi} = A_i + jB_i \quad (5)$$

Similarly, the Thevenin voltage is given by,

$$\vec{v}_{Thi} = \|V_{Thi}\|_2 \angle \delta_{Thi} = \|V_{Thi}\|_2 \cos(\delta_{Thi}) + j \|V_{Thi}\|_2 \sin(\delta_{Thi}) \quad (6)$$

To relate the local PCC voltage ( $\vec{v}_{PCCi}$ ) to the dispatched PQ set-points of the  $i^{th}$  targeted grid-feeding inverter; the local PCC current ( $\vec{i}_{PCCi}$ ) can be written as (7).

$$\begin{aligned} \vec{i}_{PCCi} &= \left( (P_i^{Ref} - PLi) - j(Q_i^{Ref} - QLi) \right) \vec{v}_{PCCi}^{*-1} \\ &= (P_{PCCi} - jQ_{PCCi}) \vec{v}_{PCCi}^{*-1} \end{aligned} \quad (7)$$

where  $\vec{v}_{PCCi}^*$  is the complex conjugate of  $\vec{v}_{PCCi}$ ,  $P_i^{Ref}$  is the dispatched active power reference by the  $i^{th}$  targeted grid-feeding inverter,  $Q_i^{Ref}$  is the dispatched reactive power reference  $i^{th}$  targeted grid-feeding inverter,  $PLi$  is the active power

load at the  $i^{th}$  targeted local PCC bus,  $QLi$  is the reactive power load at the  $i^{th}$  targeted local PCC bus,  $P_{PCCi}$  is the net injected active power at the  $i^{th}$  targeted local PCC bus, and  $Q_{PCCi}$  is the net injected reactive power at the  $i^{th}$  targeted local PCC. Combining (7) and (4) results in (8).

$$\vec{v}_{PCCi} = (R_{Thi} + j\omega L_{Thi}) (P_{PCCi} - jQ_{PCCi}) \vec{v}_{PCCi}^{*-1} + \vec{v}_{Thi} \quad (8)$$

Then, multiplying (6) by the complex conjugate of  $\vec{v}_{PCCi}$  results in (9).

$$\vec{v}_{PCCi} \vec{v}_{PCCi}^* = (R_{Thi} + j\omega L_{Thi}) (P_{PCCi} - jQ_{PCCi}) + \vec{v}_{Thi} \vec{v}_{PCCi}^* \quad (9)$$

The key point from reaching to (9) is that the left-hand side (LHS) is all real valued terms. In other words, the imaginary part is zero. This is an obvious resultant form multiplication of the local PCC phasor voltage by its complex conjugate. Thereby, (9) can be rewritten as (10).

$$\begin{aligned} A_i^2 + B_i^2 &= R_{Thi} P_{PCCi} + \omega L_{Thi} Q_{PCCi} \\ &+ \|V_{Thi}\|_2 (A_i \cos(\delta_{Thi}) + B_i \sin(\delta_{Thi})) \\ &+ j(\omega L_{Thi} P_{PCCi} - R_{Thi} Q_{PCCi} \\ &+ \|V_{Thi}\|_2 (A_i \sin(\delta_{Thi}) - B_i \cos(\delta_{Thi}))) \end{aligned} \quad (10)$$

Then, by equating the real parts of the LHS and right-hand side (RHS) of (10); (11) is deduced.

$$\begin{aligned} A_i^2 + B_i^2 &= R_{Thi} P_{PCCi} + \omega L_{Thi} Q_{PCCi} + A_i \|V_{Thi}\|_2 \cos(\delta_{Thi}) \\ &+ B_i \|V_{Thi}\|_2 \sin(\delta_{Thi}) \end{aligned} \quad (11)$$

Similarly, by equating the imaginary parts of the LHS and RHS of (10); (12) is obtained.

$$\begin{aligned} 0 &= \omega L_{Thi} P_{PCCi} - R_{Thi} Q_{PCCi} + A_i \|V_{Thi}\|_2 \sin(\delta_{Thi}) \\ &- B_i \|V_{Thi}\|_2 \cos(\delta_{Thi}) \end{aligned} \quad (12)$$

Now, from (11) and (12) a solution of  $A_i$  and  $B_i$  parameters can be determined. Recall that these parameters construct the real and the imaginary component of the  $i^{th}$  targeted local PCC voltage given previously by (5).  $B_i$  is written in term of  $A_i$  from (12) as expressed in (13).

$$\begin{aligned} B_i &= (\omega L_{Thi} P_{PCCi} - R_{Thi} Q_{PCCi}) \|V_{Thi}\|_2^{-1} \sec(\delta_{Thi}) \\ &+ A_i \tan(\delta_{Thi}) \end{aligned} \quad (13)$$

For finding a solution for  $A_i$ ; from combining (13) and (11) this parametric quadratic equation expressed in (14) can be solved.

$$\begin{aligned} A_i^2 - A_i &\left( 2(R_{Thi} Q_{PCCi} - \omega L_{Thi} P_{PCCi}) \right. \\ &\times \|V_{Thi}\|_2^{-1} \sin(\delta_{Thi}) + \|V_{Thi}\|_2 \cos(\delta_{Thi}) \left. \right) \\ &+ \left( (\omega L_{Thi} P_{PCCi} - R_{Thi} Q_{PCCi}) \|V_{Thi}\|_2^{-1} \right)^2 \\ &- (R_{Thi} P_{PCCi} + \omega L_{Thi} Q_{PCCi}) \cos^2(\delta_{Thi}) \\ &- (\omega L_{Thi} P_{PCCi} - R_{Thi} Q_{PCCi}) \cos(\delta_{Thi}) \sin(\delta_{Thi}) = 0 \end{aligned} \quad (14)$$

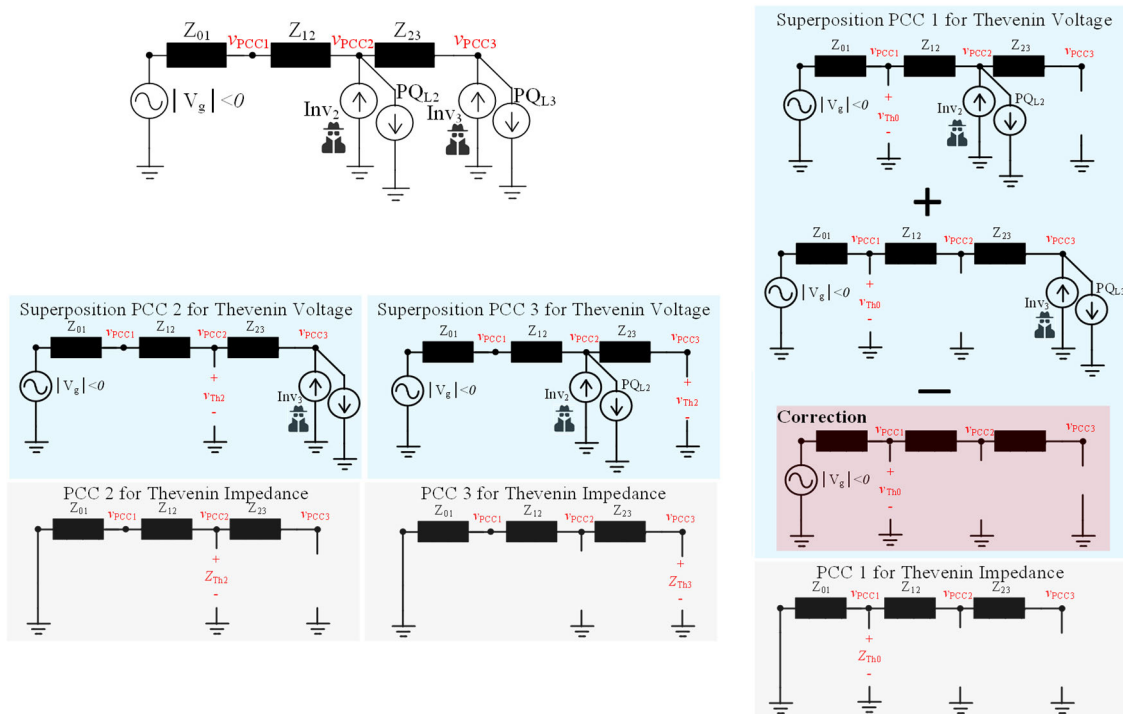


FIGURE 5. Four bus single-phase PEDG considered for illustrating the operation regions graphically in scenario I.

where

$$\begin{aligned}
 a &= 1, \\
 b &= - \left( 2 (R_{Thi} Q_{PCCi} - \omega L_{Thi} P_{PCCi}) \right. \\
 &\quad \times \|V_{Thi}\|_2^{-1} \sin(\delta_{Thi}) + \|V_{Thi}\|_2 \cos(\delta_{Thi}) \left. \right), \\
 c &= \left( (\omega L_{Thi} P_{PCCi} - R_{Thi} Q_{PCCi}) \|V_{Thi}\|_2^{-1} \right)^2 \\
 &\quad - (R_{Thi} P_{PCCi} + \omega L_{Thi} Q_{PCCi}) \cos^2(\delta_{Thi}) \\
 &\quad - (\omega L_{Thi} P_{PCCi} - R_{Thi} Q_{PCCi}) \cos(\delta_{Thi}) \sin(\delta_{Thi})
 \end{aligned}$$

Theoretically, equation (14) has two bifurcation solutions. However, only the solution with a positive sign root is practical. This is because if the grid-feeding inverter is not injecting any current at its local PCC terminals, the local PCC voltage must be equal to the Thevenin voltage. While the impractical solution is giving a contradictory result of  $\vec{v}_{PCCi} = 0$ . The solution for  $A_i$  is given in (15), as shown at the bottom of the next page.

Furthermore, the solution for  $B_i$  is given in (16), as shown at the bottom of the next page, now,  $\|\vec{v}_{PCCi}\|_2 = \sqrt{A_i^2 + B_i^2}$  describes the SOR of the  $i^{th}$  targeted local PCC bus in a three-dimensional surface for a given Thevenin representation of the rest of network. In this case, the SOR of the targeted  $i^{th}$  PCC bus is the projection of the surface on the  $P_{PCCi}$  and  $Q_{PCCi}$  plane where  $\|\vec{v}_{PCCi}\|_2 \in \mathbb{R}$ . Also, subspace of the stable/normal operation region (SNOR) is described by projection of the surface with co-domain of  $\|\vec{v}_{PCCi}\|_2 \|v_g\|_2^{-1} \in [0.8, 1.2]$  on the  $P_{PCCi}$  and  $Q_{PCCi}$  plane. On the other hand,

any operation set-points that satisfies  $\|\vec{v}_{PCCi}\|_2 \notin \mathbb{R}$  is in the UOR (see the proof in appendix D). Yet, these operation regions cannot be utilized. As finding the Thevenin voltage of the rest of the network requires repeated load flow solutions.

To extend this analysis to closed-form, the inclusion of nearby PCC buses PQ set-points on the  $i^{th}$  targeted PCC bus is deliberated by finding the expression of the Thevenin voltage in (6) as a function of all the other grid-feeding inverters PQ set-points except the targeted  $i^{th}$  grid-feeding inverter. In fact, with such consideration the targeted PCC voltage is expressed with a multi-dimensional manifold. This process is repeated for every local PCC bus in the network and then the intersection of all PCC buses SOR is considered as the whole PEDG SOR (i.e., *Morphism 2* expressed in (3)) Note that, *Morphism 2* closed-form is developed mathematically in the next subsection. Whereas, *Morphism 1* that is expressed in (2)) cannot be derived in closed-form its  $\mathbb{R} \rightarrow \mathbb{R}^{2N}$  mapping structure preservation is measured through observing the imaginary-part of the PCC voltage  $L_2$  norm.

### C. GRAPHICAL EXAMPLE OF MORPHISM 2 DERIVATION

The inclusion of nearby grid-feeding inverters (i.e., DEGs) influence is determined by finding the closed form solution of the Thevenin voltage depicted (4)-(16). To understand this, an example is taken here of the PEDG network shown in Fig. 5. This example can be extended to any network with an arbitrary number of grid-feeding inverters. In this case, the Thevenin voltage of the grid-feeding inverter at local PCC bus

2 is as (17), shown at the bottom of the next page. Then, this Thevenin voltage is combined with (15) and (16) considering the index  $i$  equal to 2.

Similarly, the voltage at the local PCC bus 3 is a function of all PQ set-points in the network and can be described by (15) and (16) with index  $i$  equal to 3 and (18), as shown at the bottom of the next page.

Also, the voltage at main PEDG bus is a function of all PQ set-points in the network and described by (19).

$$\begin{aligned} \|\vec{v}_{PCC1}\|_2 &= \left\| (\vec{v}_{Bus2} - \vec{v}_g) (Z_{Th0}) (Z_{Th2})^{-1} \right. \\ &\quad \left. + (\vec{v}_{Bus3} - \vec{v}_g) (Z_{Th0}) (Z_{Th3})^{-1} + \vec{v}_g \right\|_2 \\ Z_{Th0} &= Z_{01}, R_{Th0} = Re \{Z_{Th0}\}, L_{Th2} = Im \{Z_{Th0}\} \omega^{-1} \end{aligned} \quad (19)$$

In this example, each PCC bus is five dimensional manifold. A correction is needed in finding the main PEDG multi-dimensional manifold. This correction is related to the usage of the source  $\vec{v}_g$  twice in the superposition analysis. Furthermore, this correction is depicted graphically in Fig. 5. This correction can be applied to any general network architecture radial or mesh. In fact, a more complex PEDG network is taken as an example to illustrate this correction on superposition theory application for obtaining local PCC bus 2 Thevenin voltage in Fig. 6. Furthermore, the Thevenin voltage for local PCC bus 2 is summation of  $\vec{v}_{Th2}$  in all the five equivalent circuits shown in Fig. 7. However, the correction in this example is to subtract four times the impact of  $\vec{v}_g$  on the local PCC bus 2. This approach allows obtaining local PCC bus 2 as a function of all PEDG PQ set-points. Note that, this analysis focused on superposition is because the basis of this analysis is on repetitive utilization of subsection III.B results.

Without loss of generality, let us consider  $Q_{PCC2}$  and  $Q_{PCC3}$  are zero. Then, the realization of the different operation regions for each local PCC bus in Fig. 5 is reduced from a five-dimensional manifold to a three-dimensional surface depicted in Fig. 8(a), (b) and (c) for each PCC bus. Let  $\Omega_{SOR_1}$  be the projection of the surface  $\vec{v}_{PCC1}$  on the  $P_{PCC2}$  and  $P_{PCC3}$  plane. Then, SOR for PCC<sub>1</sub> bus described by (20).

$$\begin{aligned} \Omega_{SOR_1} &\triangleq Proj_{P_2, Q_2, P_3, Q_3} \left( \|\vec{v}_{PCC1}\|_2 \right) \|\vec{v}_{PCC1}\|_2 \in \mathbb{R}; \\ &\quad \forall P_2, Q_2, P_3, Q_3 \in \mathbb{R} \end{aligned} \quad (20)$$

Similarly, SORs ( $\Omega_{SOR_2}$ ) and ( $\Omega_{SOR_3}$ ) for PCC2 and PCC3 are described in (21) and (22), respectively.

$$\begin{aligned} \Omega_{SOR_2} &\triangleq Proj_{P_2, Q_2, P_3, Q_3} \left( \|\vec{v}_{PCC2}\|_2 \right) \|\vec{v}_{PCC2}\|_2 \in \mathbb{R}; \\ &\quad \forall P_2, Q_2, P_3, Q_3 \in \mathbb{R} \end{aligned} \quad (21)$$

$$\begin{aligned} \Omega_{SOR_3} &\triangleq Proj_{P_2, Q_2, P_3, Q_3} \left( \|\vec{v}_{PCC3}\|_2 \right) \|\vec{v}_{PCC3}\|_2 \in \mathbb{R}; \\ &\quad \forall P_2, Q_2, P_3, Q_3 \in \mathbb{R} \end{aligned} \quad (22)$$

The SNORs of each PCC bus (i.e.,  $\Omega_{SNOR_1}$ ,  $\Omega_{SNOR_2}$ , and  $\Omega_{SNOR_3}$ ) is a subspace of the SOR described by (23)-(25).

$$\begin{aligned} \Omega_{SNOR_1} &\triangleq Proj_{P_2, Q_2, P_3, Q_3} \left( \|\vec{v}_{PCC1}\|_2 \right) \|\vec{v}_{PCC1}\|_2 \\ &\quad \times \|\vec{v}_g\|_2^{-1} \in [0.8, 1.2] \quad \forall P_2, Q_2, P_3, Q_3 \in \mathbb{R} \end{aligned} \quad (23)$$

$$\begin{aligned} \Omega_{SNOR_2} &\triangleq Proj_{P_2, Q_2, P_3, Q_3} \left( \|\vec{v}_{PCC2}\|_2 \right) \|\vec{v}_{PCC2}\|_2 \\ &\quad \times \|\vec{v}_g\|_2^{-1} \in [0.8, 1.2] \quad \forall P_2, Q_2, P_3, Q_3 \in \mathbb{R} \end{aligned} \quad (24)$$

$$\begin{aligned} \Omega_{SNOR_3} &\triangleq Proj_{P_2, Q_2, P_3, Q_3} \left( \|\vec{v}_{PCC3}\|_2 \right) \|\vec{v}_{PCC3}\|_2 \\ &\quad \times \|\vec{v}_g\|_2^{-1} \in [0.8, 1.2] \quad \forall P_2, Q_2, P_3, Q_3 \in \mathbb{R} \end{aligned} \quad (25)$$

Therefore, the network SOR ( $\Omega_{SOR}$ ) is given by (26).

$$\Omega_{SOR} \triangleq \Omega_{SOR_1} \cap \Omega_{SOR_2} \cap \Omega_{SOR_3} \quad (26)$$

$$\begin{aligned} A_i &= 0.5 \|V_{Thi}\|_2 \cos(\delta_{Thi}) + (R_{Thi}Q_{PCCi} - \omega L_{Thi}P_{PCCi}) \|V_{Thi}\|_2^{-1} \sin(\delta_{Thi}) \\ &\quad + \sqrt{0.25 \|V_{Thi}\|_2^2 \cos^2(\delta_{Thi}) + \left( (\omega L_{Thi}P_{PCCi} - R_{Thi}Q_{PCCi}) \|V_{Thi}\|_2^{-1} \right)^2 \sin^2(\delta_{Thi})} \\ &\quad + (\omega L_{Thi}P_{PCCi} - R_{Thi}Q_{PCCi}) \cos(\delta_{Thi}) \sin(\delta_{Thi}) \\ &\quad - \left( (\omega L_{Thi}P_{PCCi} - R_{Thi}Q_{PCCi}) \|V_{Thi}\|_2^{-1} \right)^2 \\ &\quad + (R_{Thi}P_{PCCi} + \omega L_{Thi}Q_{PCCi}) \cos^2(\delta_{Thi}) \end{aligned} \quad (15)$$

$$\begin{aligned} B_i &= (\omega L_{Thi}P_{PCCi} - R_{Thi}Q_{PCCi}) \|V_{Thi}\|_2^{-1} \sec(\delta_{Thi}) + 0.5 \|V_{Thi}\|_2 \sin(\delta_{Thi}) \\ &\quad + (R_{Thi}Q_{PCCi} - \omega L_{Thi}P_{PCCi}) \|V_{Thi}\|_2^{-1} \sin(\delta_{Thi}) \tan(\delta_{Thi}) \\ &\quad + \tan(\delta_{Thi}) \sqrt{0.25 \|V_{Thi}\|_2^2 \cos^2(\delta_{Thi}) + \left( (\omega L_{Thi}P_{PCCi} - R_{Thi}Q_{PCCi}) \|V_{Thi}\|_2^{-1} \right)^2 \sin^2(\delta_{Thi})} \\ &\quad + (\omega L_{Thi}P_{PCCi} - R_{Thi}Q_{PCCi}) \cos(\delta_{Thi}) \sin(\delta_{Thi}) \\ &\quad - \left( (\omega L_{Thi}P_{PCCi} - R_{Thi}Q_{PCCi}) \|V_{Thi}\|_2^{-1} \right)^2 \\ &\quad + (R_{Thi}P_{PCCi} + \omega L_{Thi}Q_{PCCi}) \cos^2(\delta_{Thi}) \end{aligned} \quad (16)$$

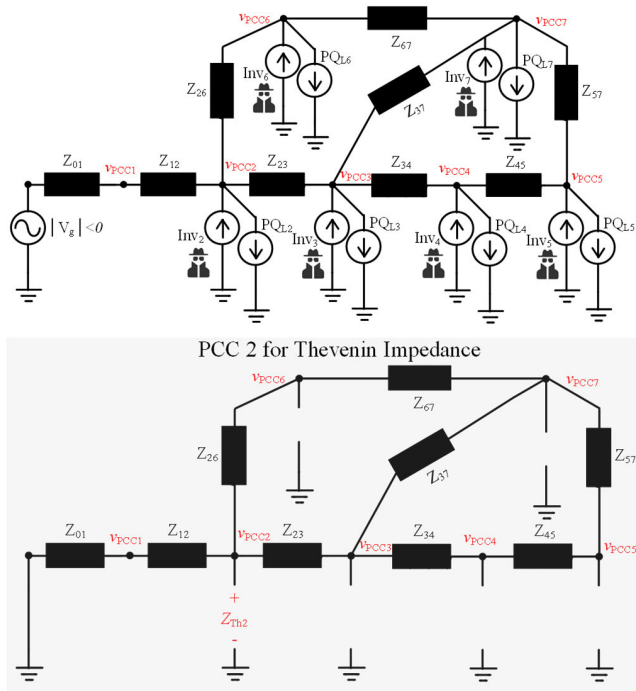


**FIGURE 6.** Eight bus single-phase PEDG example and the Thevenin impedance of PCC2.

Then, the subspace of the network SNOR ( $\Omega_{SNOR}$ ) is as (27).

$$\Omega_{SNOR} \triangleq \Omega_{SNOR1} \cap \Omega_{SNOR2} \cap \Omega_{SNOR3} \quad (27)$$

The network SOR ( $\Omega_{SOR}$ ) is depicted in Fig. 8(d) and the network SNOR ( $\Omega_{SNOR}$ ) is depicted by the green area in Fig. 8(d).

#### IV. CYBER INTRUSION DETECTION SYSTEM AND SITUATIONAL AWARENESS IMPROVEMENT BASED ON MORPHISM 1 AND MORPHISM 2

Summary of the designed IDS at the primary layer is illustrated in Fig. 3. This IDS is leveraging the developed SOR.

**TABLE 1.** Individual grid-feeding inverter DEGs ratings.

Parameter	Symbol	Value
Rated Power	$S_{Rated}$	20 kVA
Switching Frequency	$f_{sw}$	10 kHz
Nominal Grid Frequency	$\omega$	376.8 rad/s
Voltage Peak	$V_g$	171 V
DC-Bus Voltage	$V_{DCi}$	420 V
DC-link Capacitor	$C_{DCi}$	2 mF
Filter Inductor	$L_i$	0.5 mH
Filter Inductor Resistance	$R_i$	0.05 $\Omega$

Initially, an anomalous  $i^{th}$  local PCC voltage is considered by the voltage monitoring system once the *Morphism 1* is violated. Meaning that, a non-zero imaginary-part in the PCC voltage  $L_2$  norm is observed. Hence, the *morphism 2* is not producing  $\mathbb{R} \rightarrow \mathbb{R}^{2N}$  mapping. Remember that it is not possible to derive a closed-form compact solution for *Morphism 1*. Recall that,  $L_2$  norm properties nonnegativity, definiteness, triangle inequality, and homogeneity must be satisfied in SOR for PCC voltage (see Appendix D for the proof). In fact, inspecting the non-zero imaginary-part test validates holding nonnegativity property of the PCC voltage  $L_2$  norm and the mapping structure preservation. *Morphism 2* is utilized for independent decision making at the primary layer of the DEG during cyber intrusion scenarios. *Morphism 2* is an alternative for the secondary layer when the dispatched set-points are not trusted. In fact, directly after detection of an anomaly by *Morphism 1*, *Morphism 2*: is used to validate if the mapping is satisfying  $\mathbb{R}^{2N} \rightarrow \mathbb{R}$  in the primary layer with the closed-form solution provided in section III. If also *Morphism 2* is not providing  $\mathbb{R}^{2N} \rightarrow \mathbb{R}$  mapping; the set-points passing from the secondary layer are disregarded and the grid-feeding inverters are changing the set-points and monitor if the local

PCC voltage of the bus is regaining safe operation (i.e., move the network to SOR).

The steps to generate the analytic expression of each PCC bus in the single-phase PEDG as a function of all the network DEGs' PQ operation set-points are as follows:

$$\begin{aligned} \|\vec{v}_{PCC2}\|_2 &= \sqrt{A_2^2 + B_2^2}, \vec{v}_{Th2} = (\vec{v}_{Bus3} - \vec{v}_g) (Z_{Th2}) (Z_{Th3})^{-1} + \vec{v}_g, \vec{v}_g = \|V_g\|_2 \angle 0 \\ \vec{v}_{Bus3} &= 0.5 \|V_g\|_2 + j (R_{Th3} Q_{PCC3} - \omega L_{Th3} P_{PCC3}) \|V_g\|_2^{-1} \\ &\quad + \sqrt{0.25 \|V_g\|_2^2 - \left( (R_{Th3} Q_{PCC3} - \omega L_{Th3} P_{PCC3}) \|V_g\|_2^{-1} \right)^2 + (R_{Th3} P_{PCC3} + \omega L_{Th3} Q_{PCC3})} \\ Z_{Th2} &= Z_{01} + Z_{12}, R_{Th2} = \text{Re} \{Z_{Th2}\}, L_{Th2} = \text{Im} \{Z_{Th2}\} \omega^{-1} \\ Z_{Th3} &= Z_{01} + Z_{12} + Z_{23}, R_{Th3} = \text{Re} \{Z_{Th3}\}, L_{Th3} = \text{Im} \{Z_{Th3}\} \omega^{-1} \end{aligned} \quad (17)$$

$$\begin{aligned} \|\vec{v}_{PCC3}\|_2 &= \sqrt{A_3^2 + B_3^2}, \vec{v}_{Th3} = \vec{v}_{Bus2} \\ \vec{v}_{Bus2} &= 0.5 \|V_g\|_2 + j (R_{Th2} Q_{PCC2} - \omega L_{Th2} P_{PCC2}) \|V_g\|_2^{-1} \\ &\quad + \sqrt{0.25 \|V_g\|_2^2 - \left( (R_{Th2} Q_{PCC2} - \omega L_{Th2} P_{PCC2}) \|V_g\|_2^{-1} \right)^2 + (R_{Th2} P_{PCC2} + \omega L_{Th2} Q_{PCC2})} \end{aligned} \quad (18)$$

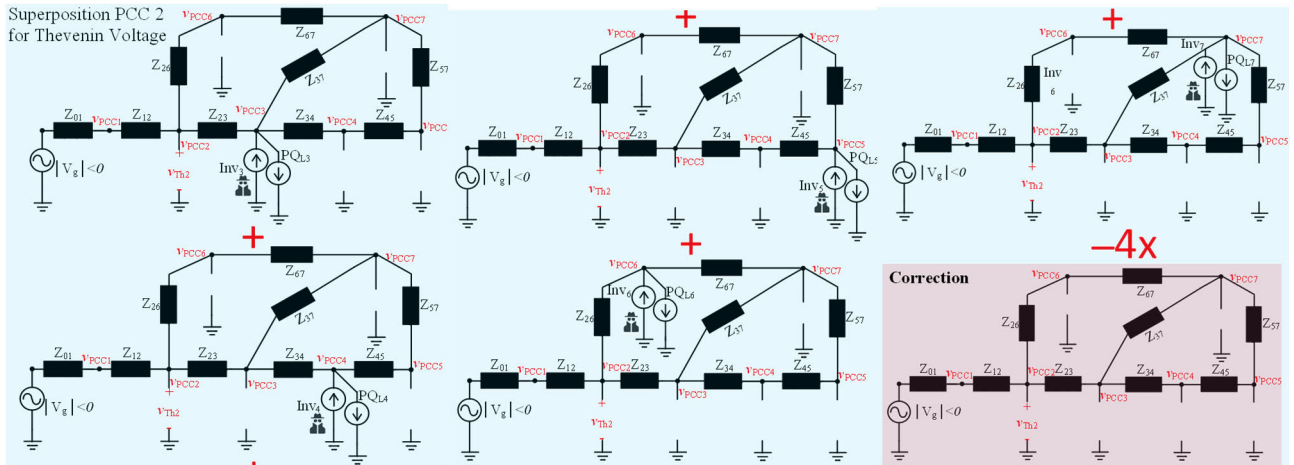


FIGURE 7. Eight bus single-phase PEDG example with the correction for Thevenin voltage on superposition theory to obtain PCC2.

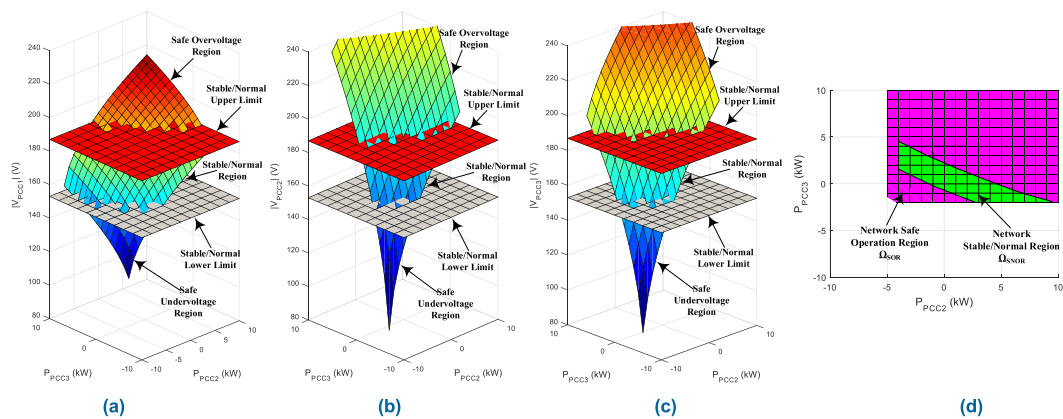


FIGURE 8. Operation regions of (a) PCC 1, (b) PCC 2, (c) PCC 3, and (d) SOR and SNOR of the four PCC bus single-phase PEDG for scenario I.

1 - Each local PCC bus can be described by (15) and (16). These equations include the remaining non-targeted PCC buses operation set-points in the Thevenin voltage expression.

2 - Then, finding the Thevenin voltage expression analytically requires application of superposition multiple times. However, a correction must be done at the end to eliminate the effect of using some sources multiple times. The repetition of these sources is used for sake of solvability. In other words, this approach is followed to utilize repetitively the analogy introduced in section III.B.

3 - After that, for each local PCC bus a multi-dimensional manifold is acquired. These manifolds are used to define the SOR of each local PCC bus when  $\|\vec{v}_{PCCi}\|_2 \in \mathbb{R}$  is satisfied (This is the developed *Morphism 2* when  $\mathbb{R}^{2N} \rightarrow \mathbb{R}$ ). This is graphically representing the projection of the manifold on the independent variables domain. Also, the subspace that defined SNOR is the projection portion of SOR where the co-domain is  $\|\vec{v}_{PCCi}\|_2 \|\vec{v}_g\|_2^{-1} \in [0.8, 1.2]$ . In addition, any operation point outside SOR is in UOR of the local PCC bus, i.e.  $\|\vec{v}_{PCCi}\|_2 \notin \mathbb{R}$ .

4 - The intersection of all local PCC SORs obtains the SOR of the whole single-phase PEDG. This SOR region is used to enable understanding compromised secondary control layer

dispatched PQ set-points that are passing to the primary control layer of the unobservable DEGs.

The challenge that might arise is what if finding the Thevenin impedance or reduction of the impedance network during each stage of superposition is non-solvable due to network connection complexity. This can be elucidated with using the general two point impedance theory introduced in [26], [27] by using the network Laplacian matrix.

### V. RESULTS AND DISCUSSION

The theoretical analyses established are validated by simulation of two scenarios. In these two scenarios, the DEGs in the multi-layer controlled PEDG network are rated according to Table 1. Particularly, the inverters representing DEGs in the PEDG are rated to 10 kVA, 60 Hz nominal frequency operation, 10 kHz switching frequency, 420 V nominal DC link voltage, and 0.5 mH filter inductor. These DEGs are controlled in grid-feeding mode of operation through the primary current control scheme illustrated above in Fig. 3.

#### A. MALICIOUS CYBER-ATTACK SCENARIO I

The malicious cyber-attack scenario depicted in Fig. 9 validates the different operation regions derived and shows the

effectiveness of using these operation regions for intrusion detection. Initially, the single-phase PEDG of Fig. 5 is operating in the network SNOR with  $P_{PCC2} = 2$  kW,  $P_{PCC3} = -1$  kW (see Fig. 9 from 0.1 s to 0.2 s). Then, the intruder manipulates the DEGs operation set-points passing from the secondary control layer by utilizing the reserved generation (i.e. PV power reserve, or energy storage) at PCC2. The new operation set-points results in surplus of 4 kW at PCC2 bus (see Fig. 9 from 0.2 s to 0.3 s). At this duration, the PEDG is moved to the overvoltage SOR and the attacker fails to jeopardize the operation of the network also the IDS is not performing any action as no anomalous voltage is observed. After that, at time instant 0.3 s in Fig. 9 the attacker manipulates the generation at PCC2 and PCC3 by reducing the generation so the net power appearing at PCC2 and PCC3 is  $-5$  kW. Now, the PEDG is witnessing unstable operation seen in the voltage waveforms, power oscillations, and overcurrent after 0.3 s in Fig. 9. In this situation, the IDS catches through *Morphism 2* and *Morphism 1* mapping nature that the last operation set-points belong to the UOR. After that, PCC2 and PCC3 grid-feeding inverter are controlling their local PCC voltage through the set-points and disregard the PEDG secondary layer dispatched set-points after 0.4 s in Fig. 9. The new operation PQ set-points are obtained by using the generation reserved at PCC2 and PCC3 to 2 kW and 4 kW. As consequence, the PEDG regains operation in the undervoltage SOR after 0.4 s in Fig. 9.

**B. MALICIOUS CYBER-ATTACK SCENARIO II**

Now, for the scenario of the PEDG with seven buses that is shown in Fig. 10, each local PCC bus is described with

eleven dimensional manifolds. Furthermore, in this scenario initially the PEDG is operating in the SNOR of the network (see Fig. 11 before time instant 0.3 s). All consumers DEGs are meeting their local loads and not injecting any power into their local PCC terminals. After that, power reversal occurs at PCC2 and PCC3 after time instant 0.3 s in Fig. 11 due to a manipulation by a cyber intruder at the secondary layer. At this duration, the set-points 2 kW for PCC2 4 kW for PCC3 belong to the SOR and the intruder fails to jeopardize the network operation. Then, after 0.4 s in Fig. 11, PCC2 and PCC3 are pushed to unstable operation by the intruder. This new operation set-point  $-5$  kW for PCC2 and PCC3 are in the UOR and the intruder is successful to induce an unstable operation. The IDS will alert the DEG that an anomalous voltage is detected, then the DEGs are moved to local primary control mode based on PCC voltage condition to push the PEDG to the SNOR (see Fig. 11 after time instant 0.5 s). For this example, the local PCC buses and the main PEDG bus eleven dimensional manifolds are described by (28)–(33), as shown at the bottom of the page.

The SOR and SNOR of each PCC bus is described in (34) and (35), as shown at the bottom of the page, respectively.

$$\Omega_{SOR_i} \triangleq \text{Proj}_{P_2, Q_2, \dots, P_6, Q_6} (\|\vec{v}_{PCC_i}\|_2) \mid \|\vec{v}_{PCC_i}\|_2 \in \mathbb{R}; \quad \forall P_2, Q_2, \dots, P_6, Q_6 \in \mathbb{R} \quad (34)$$

$$\Omega_{SNOR_i} \triangleq \text{Proj}_{P_2, Q_2, \dots, P_6, Q_6} (\|\vec{v}_{PCC_i}\|_2) \mid \|\vec{v}_{PCC_i}\|_2 \times \|\vec{v}_g\|_2^{-1} \in [0.8, 1.2]; \quad \forall P_2, Q_2, \dots, P_6, Q_6 \in \mathbb{R} \quad (35)$$

$$\|\vec{v}_{PCC1}\|_2 = \left\| \vec{v}_g + \sum_{i=2}^6 (\vec{v}_{Busi} - \vec{v}_g) (Z_{Th0}) (Z_{Thi})^{-1} \right\|_2, \quad \vec{v}_g = |V_g| \angle 0 \quad (28)$$

$$\vec{v}_{Busi} = 0.5 \|V_g\|_2 + j (R_{Thi} Q_{PCCi} - \omega L_{Thi} P_{PCCi}) \|V_g\|_2^{-1} + \sqrt{0.25 \|V_g\|_2^2 - ((R_{Thi} Q_{PCCi} - \omega L_{Thi} P_{PCCi}) \|V_g\|_2^{-1})^2 + (R_{Thi} P_{PCCi} + \omega L_{Thi} Q_{PCCi})}$$

$$Z_{Thi} = \sum_{x=0, y=1}^{x=N-1, y=N} Z_{xy}, \quad R_{Thi} = \text{Re} \{Z_{Thi}\}, \quad L_{Thi} = \text{Im} \{Z_{Thi}\} \omega^{-1}, \quad N = 6$$

$$\|\vec{v}_{PCC2}\|_2 = \sqrt{A_2^2 + B_2^2}, \quad \vec{v}_{Th2} = \vec{v}_g + \sum_{i=3}^6 (\vec{v}_{Busi} - \vec{v}_g) (Z_{Th2}) (Z_{Thi})^{-1} \quad (29)$$

$$\|\vec{v}_{PCC3}\|_2 = \sqrt{A_3^2 + B_3^2}, \quad \vec{v}_{Th3} = \vec{v}_{Bus2} + \sum_{i=4}^6 (\vec{v}_{Busi} - \vec{v}_g) (Z_{Th3}) (Z_{Thi})^{-1} \quad (30)$$

$$\|\vec{v}_{PCC4}\|_2 = \sqrt{A_4^2 + B_4^2}, \quad \vec{v}_{Th4} = \vec{v}_{Bus2} + \vec{v}_{Bus3} - \vec{v}_g + \sum_{i=5}^6 (\vec{v}_{Busi} - \vec{v}_g) (Z_{Th4}) (Z_{Thi})^{-1} \quad (31)$$

$$\|\vec{v}_{PCC5}\|_2 = \sqrt{A_5^2 + B_5^2}, \quad \vec{v}_{Th5} = (\vec{v}_{Bus6} - \vec{v}_g) (Z_{Th5}) (Z_{Th6})^{-1} - 2\vec{v}_g + \sum_{i=2}^4 \vec{v}_{Busi} \quad (32)$$

$$\|\vec{v}_{PCC6}\|_2 = \sqrt{A_6^2 + B_6^2}, \quad \vec{v}_{Th6} = -3\vec{v}_g + \sum_{i=2}^5 \vec{v}_{Busi} \quad (33)$$

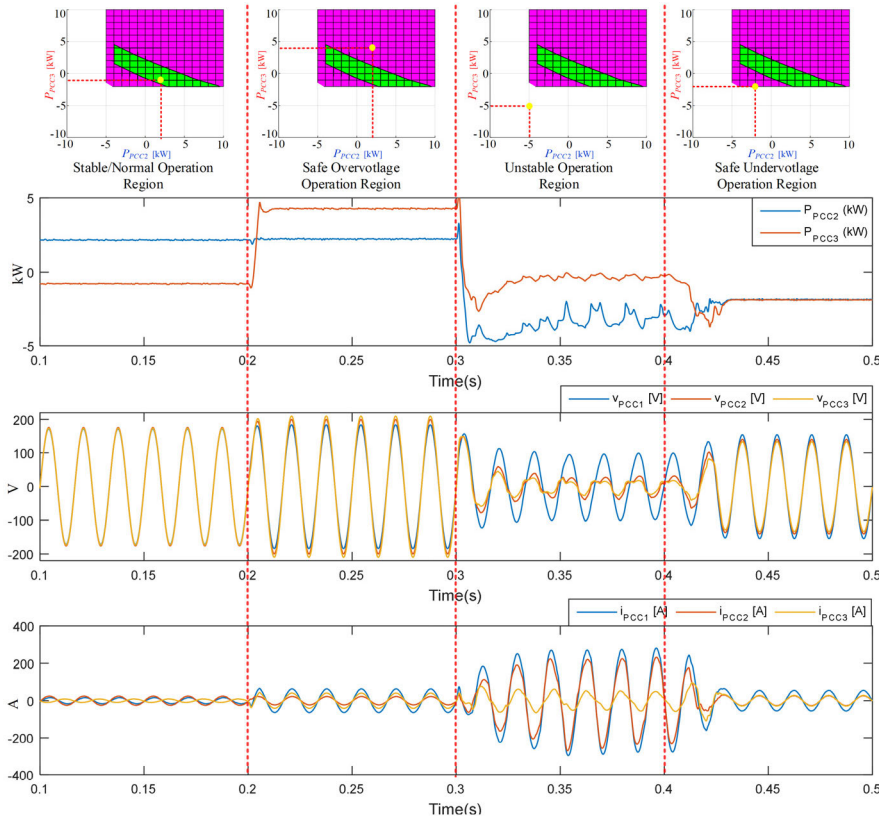


FIGURE 9. Scenario I effectiveness using the identified real-time operation regions for intrusion detection in PEDG of Figure 5.

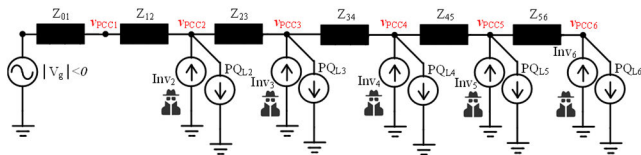


FIGURE 10. Seven bus single phase PEDG for scenario II.

Consequently, the network SOR ( $\Omega_{SOR}$ ) is given by (36).

$$\Omega_{SOR} \triangleq \Omega_{SOR_1} \cap \Omega_{SOR_2} \cap \Omega_{SOR_3} \cap \Omega_{SOR_4} \cap \Omega_{SOR_5} \cap \Omega_{SOR_6} \quad (36)$$

Then, the subspace of the network SNOR ( $\Omega_{SNOR}$ ) is as (37).

$$\Omega_{SNOR} \triangleq \Omega_{SNOR_1} \cap \Omega_{SNOR_2} \cap \Omega_{SNOR_3} \cap \Omega_{SNOR_4} \cap \Omega_{SNOR_5} \cap \Omega_{SNOR_6} \quad (37)$$

Based on (28)-(37) the operation regions are depicted in Fig. 12 for scenario II.

It worth mentioning that once the IDS identified malicious PQ set-point and the DEG disregard the secondary layer controller set-point assignment, the DEG network may not operate in optimal operation set-point anymore which was the task of secondary layer controller, but it prevents the collapse of the network which may have catastrophic impact on the PEDG. Thus, the objective of the proposed approach is prevention of the catastrophic grid failure and large blackouts by intrusion detection at early stage while the grid operates

are being alerted for further diagnosis, devices and controllers reset, etc.

## VI. CONCLUSION

The overall objective of this article is to realize an IDS for a multi-layer controlled PEDG to improve the situational awareness feature. This situational awareness enhancement results in improved cybersecurity against malicious set-points requests for the upper layer. Firstly, a mathematical theory is developed for deriving a safe operation region for multiple point of common coupling (PCC) buses. This mathematical theory extends the stability margins deduced from P-V curves to generalized morphisms. Particularly, there are two morphisms for each PCC bus when operating in the safe operation region: (*Morphism 1*) PCC bus voltage mapped to network set-points that is  $\mathbb{R}$  to  $\mathbb{R}^{2N}$  mapping, and (*Morphism 2*) network set-points mapped to the PCC bus voltage that is  $\mathbb{R}^{2N}$  to  $\mathbb{R}$  mapping. *Morphism 1* is used for anomaly detection originating from the secondary layer dispatched set-points manipulation. Explicitly, observation of a non-zero imaginary-part in the PCC voltage  $L_2$  norm is evidence of an anomaly. *Morphism 2* is utilized for independent decision making at the primary layer of the DEG during cyber intrusion scenarios. In other words, *Morphism 2* is an alternative for the secondary layer when the dispatched set-points are not trusted. Finally, two scenarios were simulated illustrating the effectiveness of the proposed theory.

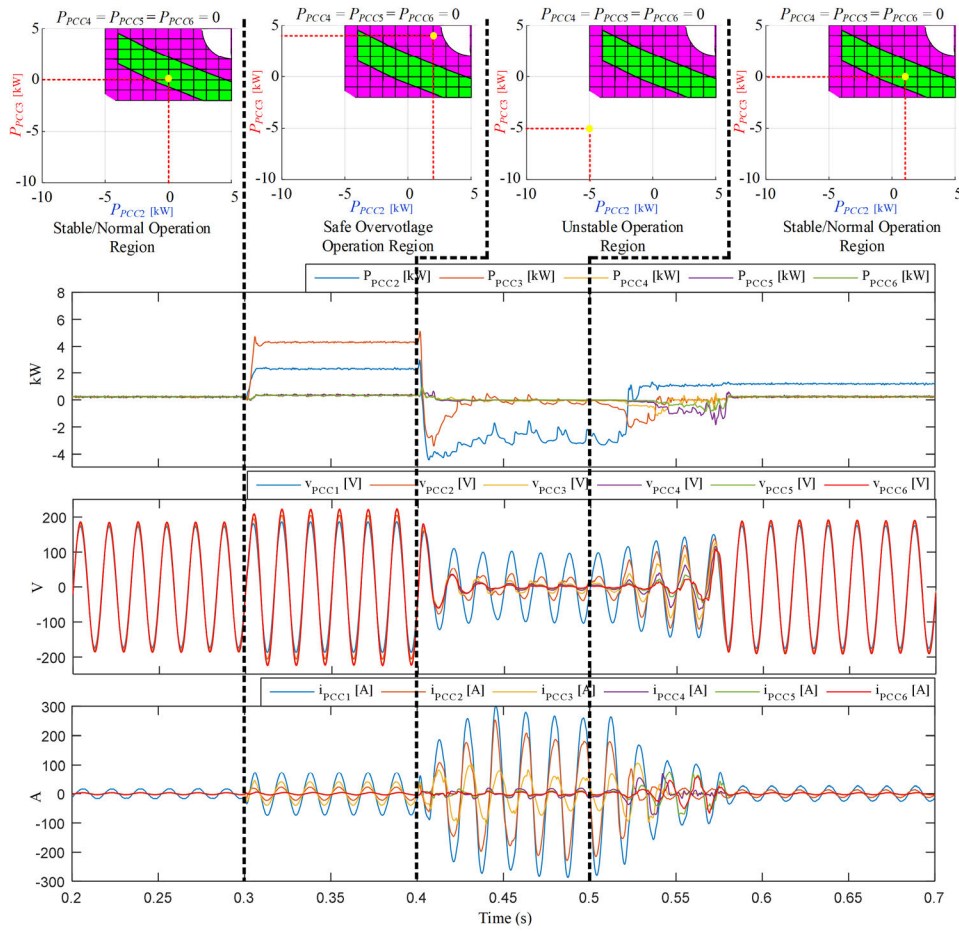


FIGURE 11. Scenario II for the seven bus single-phase PEDG shown in Figure 10 the PEDG operator is utilizing the operation regions after detecting anomalous voltage at PCC2 and PCC3.

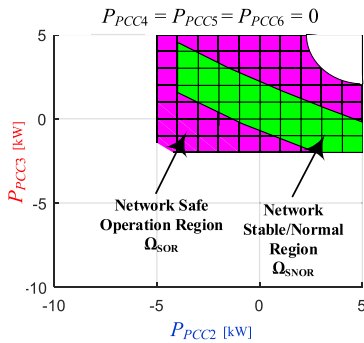


FIGURE 12. Seven bus single phase PEDG for scenario II operation regions.

### APPENDIX A STABILITY OF THE $i^{th}$ GRID-FEEDING INVERTER PRIMARY LAYER USED FOR DEGS IN THE SINGLE-PHASE PEDG

Consider the  $i^{th}$  single-phase grid-feeding inverter that is connected to its local PCC terminals in Fig. 1. The active power ( $P_i$ ) and reactive power ( $Q_i$ ) injected into the network by this inverter can be measured by using the second order generalized integrator (SOGI) presented as (A.1) and (A.2),

respectively.

$$P_i = \frac{i_{PCCi}^\alpha v_{PCCi}^\alpha}{2} + \frac{i_{PCCi}^\beta v_{PCCi}^\beta}{2} \quad (A.1)$$

$$Q_i = \frac{i_{PCCi}^\alpha v_{PCCi}^\beta}{2} - \frac{i_{PCCi}^\beta v_{PCCi}^\alpha}{2} \quad (A.2)$$

By differentiating equations (A.1) and (A.2), the state-space model that includes active and reactive power as state variables can be determined,

$$\begin{aligned} \frac{dP_i}{dt} &= \frac{v_{PCCi}^\alpha}{2} \frac{di_{PCCi}^\alpha}{dt} + \frac{i_{PCCi}^\alpha}{2} \frac{dv_{PCCi}^\alpha}{dt} + \frac{v_{PCCi}^\beta}{2} \frac{di_{PCCi}^\beta}{dt} \\ &\quad + \frac{i_{PCCi}^\beta}{2} \frac{dv_{PCCi}^\beta}{dt} \end{aligned} \quad (A.3)$$

$$\begin{aligned} \frac{dQ_i}{dt} &= \frac{v_{PCCi}^\beta}{2} \frac{di_{PCCi}^\alpha}{dt} + \frac{i_{PCCi}^\alpha}{2} \frac{dv_{PCCi}^\beta}{dt} - \frac{v_{PCCi}^\alpha}{2} \frac{di_{PCCi}^\beta}{dt} \\ &\quad \times \frac{i_{PCCi}^\beta}{2} \frac{dv_{PCCi}^\alpha}{dt} \end{aligned} \quad (A.4)$$

Furthermore, the expression for the derivatives of the stationary reference frame PCC currents  $i_{PCCi}^\alpha$  and  $i_{PCCi}^\beta$  in (A.3) and (A.4) are deduced by applying Kirchhoff voltage law at the

loop of common coupling depicted in Fig. 1. Hence, the PCC currents derivatives are as (A.5) and (A.6).

$$\frac{di_{PCCi}^\alpha}{dt} = L_i^{-1} m_i^\alpha v_{DCi} - L_i^{-1} v_{PCCi}^\alpha - L_i^{-1} R_i i_{PCCi}^\alpha \quad (A.5)$$

$$\frac{di_{PCCi}^\beta}{dt} = L_i^{-1} m_i^\beta v_{DCi} - L_i^{-1} v_{PCCi}^\beta - L_i^{-1} R_i i_{PCCi}^\beta \quad (A.6)$$

where  $m_i^\alpha$  and  $m_i^\beta$  are stationary reference frame modulation indices of the  $i^{th}$  inverter,  $L_i$  is the filter inductance of the  $i^{th}$  inverter, and  $R_i$  is the filter resistance of the  $i^{th}$  inverter. Similarly, expression of the derivatives of the stationary reference PCC voltages  $v_{PCCi}^\alpha$  and  $v_{PCCi}^\beta$  in equations (A.3) and (A.4) are given as (A.7) and (A.8).

$$\frac{dv_{PCCi}^\alpha}{dt} = -\omega v_{PCCi}^\beta \quad (A.7)$$

$$\frac{dv_{PCCi}^\beta}{dt} = \omega v_{PCCi}^\alpha \quad (A.8)$$

where  $\omega$  is the angular frequency of the network. Therefore, substituting (A.5), (A.6), (A.7) and (A.8) into (A.3) and (A.4) results in the time varying MIMO state-space system given by (A.9). The system is time varying because the stationary reference modulation indices  $m_i^\alpha$  and  $m_i^\beta$  are multiplied by the PCC voltages. In addition, this MIMO state space control inputs are coupled in both states.

$$\begin{bmatrix} \frac{dP_i}{dt} \\ \frac{dQ_i}{dt} \end{bmatrix} = \begin{bmatrix} -R_i L_i^{-1} & -\omega \\ \omega & -R_i L_i^{-1} \end{bmatrix} \begin{bmatrix} P_i \\ Q_i \end{bmatrix} + 0.5 L_i^{-1} \times \begin{bmatrix} m_i^\alpha v_{DCi} v_{PCCi}^\alpha + m_i^\beta v_{DCi} v_{PCCi}^\beta - \|\vec{v}_{PCCi}\|_2^2 \\ m_i^\alpha v_{DCi} v_{PCCi}^\beta - m_i^\beta v_{DCi} v_{PCCi}^\alpha \end{bmatrix} \quad (A.9)$$

where  $\|\vec{v}_{PCCi}\|_2^2$  is the  $L_2$  norm of  $\vec{v}_{PCCi}$ . However, if the two inputs are defined as (A.10) and (A.11), then, the state-space in (A.9) transform into a simple linear time invariant (LTI) MIMO state-space as (A.12).

$$u_{Pi} = m_i^\alpha v_{DCi} v_{PCCi}^\alpha + m_i^\beta v_{DCi} v_{PCCi}^\beta - \|\vec{v}_{PCCi}\|_2^2 \quad (A.10)$$

$$u_{Qi} = m_i^\alpha v_{DCi} v_{PCCi}^\beta - m_i^\beta v_{DCi} v_{PCCi}^\alpha \quad (A.11)$$

$$\begin{bmatrix} \frac{dP_i}{dt} \\ \frac{dQ_i}{dt} \end{bmatrix} = \begin{bmatrix} -R_i L_i^{-1} & -\omega \\ \omega & -R_i L_i^{-1} \end{bmatrix} \begin{bmatrix} P_i \\ Q_i \end{bmatrix} + 0.5 L_i^{-1} \begin{bmatrix} u_{Pi} \\ u_{Qi} \end{bmatrix} \quad (A.12)$$

now, consider the error on the instantaneous active and reactive power for the  $i^{th}$  inverter as (A.13) and (A.14),

$$e_{Pi} = P_{Refi} - P_i \quad (A.13)$$

$$e_{Qi} = Q_{Refi} - Q_i \quad (A.14)$$

where  $P_{Refi}$  is the reference commanded active power and  $Q_{Refi}$  is the reference commanded reactive power. Moreover,

the cancellation of the coupling terms in (A.12) is achieved by taking the following control law that includes feedback and feedforward as (A.15) and (A.16).

$$u_{Pi} = \underbrace{2L_i \omega Q_i}_{\text{Feedforward}} + \underbrace{2L_i v_{Pi}}_{\text{Feedback}} \quad (A.15)$$

$$u_{Qi} = \underbrace{-2L_i \omega P_i}_{\text{Feedforward}} + \underbrace{2L_i v_{Qi}}_{\text{Feedback}} \quad (A.16)$$

The feedback term  $v_P$  in (A.15) is obtained with a Proportional Integral (PI) controller as (A.16) that tracks the desired active power reference.

$$v_{Pi} = K_{Ppi} e_{Pi} + K_{Pii} \int_0^t e_{Pi}(\tau) d\tau \quad (A.17)$$

Similarly, the feedback term  $v_Q$  in (A.17) is deduced with a PI controller as (A.18), this PI controller assures tracking the desired reactive power reference.

$$v_{Qi} = K_{Qpi} e_{Qi} + K_{Qii} \int_0^t e_{Qi}(\tau) d\tau \quad (A.18)$$

Moreover, substituting (A.17) into (A.15) and then placing the resulting expression into (A.12) yields the error dynamics of the active power that is given by (A.19).

$$\frac{de_{Pi}}{dt} = -\left(K_{Ppi} + R_i L_i^{-1}\right) e_{Pi} - K_{Pii} \int_0^t e_{Pi}(\tau) d\tau \quad (A.19)$$

Likewise, inserting (A.18) into (A.16) and then substituting the resulting expression into (A.12) yields the error dynamics of the reactive power as (A.20).

$$\frac{de_{Qi}}{dt} = -\left(K_{Qpi} + R_i L_i^{-1}\right) e_{Qi} - K_{Qii} \int_0^t e_{Qi}(\tau) d\tau \quad (A.20)$$

The active and reactive power error dynamics in (A.21) and (A.22) indicate that if the controller gains  $K_{Ppi}$ ,  $K_{Pii}$ ,  $K_{Qpi}$  and  $K_{Qii}$  are positive, the primary control layer is exponentially globally asymptotically stable. This is proved by linear quadratic Lyapunov stability theorem as follows, (A.19) and (A.20) are expressed by the state-space (A.21), as shown at the bottom of the next page.

Then, to prove the stability of the closed loop control, the selection of a positive definite symmetrical matrix ( $Q_{CLi} \in \mathbb{R}^{4 \times 4}$ ), results in a positive definite symmetrical matrix ( $P_{CLi} \in \mathbb{R}^{4 \times 4}$ ) for satisfying the (A.22).

$$P_{CLi} A_{CLi} + A_{CLi}^T P_{CLi} + Q_{CLi} = 0. \quad (A.22)$$

To show this, the selection of  $Q_{CLi} = I^{4 \times 4}$  ( $I^{4 \times 4}$  is the identity matrix with dimension of  $4 \times 4$ ) which is a positive definite symmetrical matrix. The solution of (A.22) will be as given in (A.23).

$$P_{CLi} = \begin{bmatrix} \Theta_{11} & 0.5\Theta_{12} & 0 & 0 \\ -0.5\Theta_{12} & \Theta_{22} & 0 & 0 \\ 0 & 0 & \Lambda_{11} & 0.5\Lambda_{12} \\ 0 & 0 & -0.5\Lambda_{12} & \Lambda_{22} \end{bmatrix}$$

$$\begin{aligned} \Theta_{11} &= K_{Pii}^2 + (K_{Ppi} + R_i L_i^{-1})^2 + K_{Pii}, \Theta_{12} = K_{Pii}^{-1}, \\ \Theta_{22} &= K_{Pii}^{-1} (K_{Ppi} + R_i L_i^{-1})^{-1} - 1, \\ \Lambda_{11} &= K_{Qii}^2 + (K_{Qpi} + R_i L_i^{-1})^2 + K_{Qii}, \Lambda_{12} = K_{Qii}^{-1}, \\ \Lambda_{22} &= K_{Qii}^{-1} (K_{Qpi} + R_i L_i^{-1})^{-1} - 1 \end{aligned} \quad (A.23)$$

If the parameters  $K_{Ppi}$ ,  $K_{Pii}$ ,  $K_{Qpi}$  and  $K_{Qii}$  are designed respecting the conditions shown in (A.26),

$$\begin{aligned} K_{Ppi} + R_i L_i^{-1} &> 0, K_{Pii} > 0, \\ K_{Qpi} + R_i L_i^{-1} &> 0, K_{Qii} > 0 \end{aligned} \quad (A.24)$$

Then,  $P_{CLi} > 0$  (i.e., positive definite symmetrical matrix since all leading minors and the determinant are positive). Therefore, the equilibrium point  $(0, 0, 0, 0)$  is globally exponentially asymptotically stable. Hence, convergence of the error dynamics to the equilibrium point  $(0, 0, 0, 0)$  means the original system is converging to  $(P_{Refi}, 0, Q_{Refi}, 0)$  as  $t \rightarrow \infty$ . The Lyapunov candidate energy function is mathematically described in (A.25).

$$\begin{aligned} V_{CLi}(x_{CLi}) &= x_{CLi}^T P_{CLi} x_{CLi}, \\ \frac{dV_{CLi}(x_{CLi})}{dx_{CLi}} &= x_{CLi}^T (P_{CLi} A_{CLi} + A_{CLi}^T P_{CLi}) x_{CLi} \\ \therefore A_{CLi} &< 0, \quad P_{CLi} > 0 \\ \therefore V_{CLi}(x_{CLi}) &> 0, \quad \frac{dV_{CLi}(x_{CLi})}{dx_{CLi}} < 0 \end{aligned} \quad (A.25)$$

To retrieve the original system inputs which are the inverter stationary reference modulation indices  $m_i^\alpha$  and  $m_i^\beta$ ,

$$\begin{aligned} \begin{bmatrix} m_i^\alpha \\ m_i^\beta \end{bmatrix} &= \frac{1}{\|\vec{v}_{PCCi}\|_2^2} \begin{bmatrix} v_{PCCi}^\alpha & v_{PCCi}^\beta \\ v_{PCCi}^\beta & -v_{PCCi}^\alpha \end{bmatrix} \\ &\times \begin{bmatrix} (u_{Pi} + \|\vec{v}_{PCCi}\|_2) v_{DCi}^{-1} \\ u_{Qi} v_{DCi}^{-1} \end{bmatrix} \end{aligned} \quad (A.26)$$

$L_2$  norm  $\|\vec{v}_{PCCi}\|_2$  in (A.26) is  $\|\vec{v}_{PCCi}\|_2 \in \mathbb{R}$  in network stable conditions, since  $\vec{v}_{PCCi}$  is well-posed and the signals  $v_{PCCi}^\alpha$  and  $v_{PCCi}^\beta$  are always orthogonal. Finally, the modulation

index that controls the single-phase grid-feeding inverter is given as (A.27).

$$m_i = [1 \ 1] \begin{bmatrix} m_i^\alpha \\ m_i^\beta \end{bmatrix} \quad (A.27)$$

The controller structure is illustrated in Fig. 3.

### APPENDIX B IMPLICATION OF L2 NORM $\|\vec{v}_{PCCi}\|_2$ IN UNSTABLE PEDG CONDITIONS INDUCED BY CYBER INTRUDER SET-POINTS

The impact of unstable network conditions can be understood from the conditions where the  $L_2$  norm  $\|\vec{v}_{PCCi}\|_2$  of (A.26) is non-real or the existence of the active and reactive power measurement for the primary controller feedback in (A.1) and (A.2). Specifically, when there is an ill-posed local PCC voltage imposed on the terminals of the grid-feeding inverter due to a cyber-attacker requesting malicious set-points at the secondary control layer, the  $L_2$  norm expressed in (A.28) belong to the complex subspace.

$$\begin{aligned} \|\vec{v}_{PCCi}\|_2 &= \sqrt{v_{PCCi}^{\alpha 2} + v_{PCCi}^{\beta 2}} \in \mathbb{C} \\ \therefore \text{Im}\{\|\vec{v}_{PCCi}\|_2\} &\neq 0 \end{aligned} \quad (A.28)$$

$L_2$  norm  $\in \mathbb{C} \in \mathbb{C}$  means singularity, which results in non-existing stationary reference modulation indices (i.e., no solution for (A.26)). Also, with no PCC voltage, measuring the active and reactive power by (A.1) and (A.2) for the primary controller feedback will not be possible. Hence, these unstable conditions will cause PEDG DEGs operation failure. Hence, this proves that any instability witnessed in this PEDG is originated from unstable network conditions and not from the primary control layer.

### APPENDIX C MORPHISM TERMINOLOGY LINKED TO SAFE OPERATION REGION

A morphism is a structure-preserving map from one mathematical structure to another mathematical structure. In contemporary mathematics, the terminology morphism is an abstraction for any sort of mapping concept. For example, in linear algebra, the linear transformation is a special type

$$\begin{aligned} \frac{dx_{CLi}}{dt} &= A_{CLi} x_{CLi} \\ x_{CLi} &\in \mathbb{R}^4, \quad A_{CLi} \in \mathbb{R}^{4 \times 4} \\ x_{CLi} &= \begin{bmatrix} e_{Pi} & \frac{de_{Pi}}{dt} & e_{Qi} & \frac{de_{Qi}}{dt} \end{bmatrix}^T \\ A_{CLi} &= \begin{bmatrix} 0 & 1 & 0 & 0 \\ -K_{Pii} & -(K_{Ppi} + R_i L_i^{-1}) & 0 & 0 \\ 0 & 0 & 0 & 1 \\ 0 & 0 & -K_{Qii} & -(K_{Qpi} + R_i L_i^{-1}) \end{bmatrix} \end{aligned} \quad (A.21)$$

of morphism that provides a linkage between two different linear systems, in topology, a continuous function is a morphism that provides an image of a specific quantity to another quantity. For example, the voltage ( $v_R$ ) and current ( $i_R$ ) relation across a resistor ( $R$ ) are described by the two morphisms  $h$  in (A.29) and  $w$  in (A.30) that are  $\mathbb{C} \rightarrow \mathbb{C}$  mappings.

$$h : v_R \rightarrow i_R, \quad \mathbb{C} \rightarrow \mathbb{C} \quad (\text{A.29})$$

$$w : i_R \rightarrow v_R, \quad \mathbb{C} \rightarrow \mathbb{C} \quad (\text{A.30})$$

Trivially, the morphisms  $h$  and  $w$  are described deterministically in closed-form functions by Ohm's Law in (A.31) and (A.32) for a specific special case of a linear Ohmic resistor. However, the morphisms that are presented in (A.29) and (A.30) are abstraction of these structure-preserving maps from one mathematical structure ( $v_R$ ) to another mathematical structure ( $i_R$ ), or vice-versa.

$$h(i_R) = v_R = i_R R \quad (\text{A.31})$$

$$w(v_R) = i_R = v_R R^{-1} \quad (\text{A.32})$$

In other words, morphism is a generalization of all mapping used in different mathematical fields in the sense that the mathematical objects involved are not necessarily sets. In fact, the connections between them may be somewhat other than maps. Even though, intuitively the morphisms between the objects of a given category must behave equally to maps. In this article these concepts are borrowed for cyber intrusion detection and two morphisms are described that are extension of the P-V curve and its inverse in the following subsections.

### 1) MORPHISM 1 "GENERALIZATION OF THE P-V CURVE INVERSE"

For each PCC bus when operating in the SOR this property holds.

$$f : \|\vec{v}_{PCCi}\|_2 \rightarrow \langle P_{PCC1}, Q_{PCC1}, \dots, P_{PCCN}, Q_{PCCN} \rangle, \quad \mathbb{R} \rightarrow \mathbb{R}^{2N} \quad (\text{A.33})$$

(A.33) means there is some sort of mathematical mapping (i.e., morphism) that transforms the real-valued  $L_2$  norm  $\|\vec{v}_{PCCi}\|_2$  to real-valued set-points  $\langle P_{PCC1}, Q_{PCC1}, \dots, P_{PCCN}, Q_{PCCN} \rangle$ . Morphism 1 cannot be derived in closed-form. In this article, it is structure by being an  $\mathbb{R}$  to  $\mathbb{R}^{2N}$  mapping is observed from measuring the imaginary-part of the  $L_2$  norm  $\|\vec{v}_{PCCi}\|_2$ .

### 2) MORPHISM 2 "GENERALIZATION OF THE P-V CURVE"

For each PCC bus when operating in the SOR this property holds.

$$g : \langle P_{PCC1}, Q_{PCC1}, \dots, P_{PCCN}, Q_{PCCN} \rangle \rightarrow \|\vec{v}_{PCCi}\|_2, \quad \mathbb{R}^{2N} \rightarrow \mathbb{R} \quad (\text{A.34})$$

(A.34) is a generalization of the P-V curve used for stability analysis to morphism. This morphism is describing that

the set-points  $\langle P_{PCC1}, Q_{PCC1}, \dots, P_{PCCN}, Q_{PCCN} \rangle$  that are real-valued are transformed to real-valued  $L_2$  norm  $\|\vec{v}_{PCCi}\|_2$ . Morphism 2 is an alternative for the secondary layer when the dispatched set-points are not trusted.

## APPENDIX D PROOF ON L2 NORM NON-ZERO IMAGINARY VALUE INDICATES THAT THE SET-POINT REQUESTED FROM THE UPPER LAYER BELONGS TO UNSTABLE OPERATION REGION (UOR)

The theoretical proof behind having a none-zero imaginary part in the  $L_2$  norm of the local PCC voltage results in concluding that the set-points belong to unstable operation region (UOR) can be understood from the following example of Fig. 5 network. The stability margin found from a  $P - V$  curve at PCC bus  $i$  by change in it self-set-point is described here for a given Thevenin representation. Consider (A.35),

$$\|\vec{v}_{PCCi}\|_2 = \frac{\|V_{Thi}\|_2}{2} + \sqrt{\frac{\|V_{Thi}\|_2^2}{4} + R_{Thi} P_{PCCi}} \quad (\text{A.35})$$

(A.35) is an example of Morphism 2, the stability margin is found at a specific self-set-point ( $P_{PCCi}$ ) when the condition (A.36) happens.

$$\left. \frac{\partial \|\vec{v}_{PCCi}\|_2}{\partial P_{PCCi}} \right| = \infty \quad (\text{A.36})$$

Then, (A.36) is expanded to (A.37).

$$\left. \frac{\partial \|\vec{v}_{PCCi}\|_2}{\partial P_{PCCi}} \right| = \frac{R_{Thi}}{2\sqrt{\frac{\|V_{Thi}\|_2^2}{4} + R_{Thi} P_{PCCi}}} = \infty \quad (\text{A.37})$$

This means that the stability margin at bus  $i$  due to change at it self-set-point ( $P_{PCCi}$ ) is according to the following inequality shown in (A.38).

$$P_{PCCi} \geq -\frac{\|V_{Thi}\|_2^2}{4R_{Thi}}, \quad P_{Stability\ Bound} = -\frac{\|V_{Thi}\|_2^2}{4R_{Thi}} \quad (\text{A.38})$$

now, the stability margin of PCC bus  $i$  with respect to variation of the active power set-point at an adjacent bus  $j$  ( $P_{PCCj}$ ) can be deduced by the same reasoning. Following the analogy, the stability margin of PCC bus  $i$  with respect to change of the active power set-point at adjacent PCC bus  $j$  ( $P_{PCCj}$ ) is direct resultant from (A.39).

$$\frac{\partial \|\vec{v}_{PCCi}\|_2}{\partial P_{PCCj}} = \infty \quad \text{or} \quad \frac{\partial P_{PCCj}}{\partial \|\vec{v}_{PCCi}\|_2} = 0 \quad (\text{A.39})$$

Equation (A.39) is expanded into (A.40).

$$\frac{\partial \|\vec{v}_{PCCi}\|_2}{\partial P_{PCCj}} = \frac{1}{2} \frac{\partial \|V_{Thi}\|_2}{\partial P_{PCCj}} + \frac{|V_{Thi}| \frac{\partial \|V_{Thi}\|_2}{\partial P_{PCCj}}}{4\sqrt{\frac{\|V_{Thi}\|_2^2}{4} + R_{Thi} P_{PCCi}}} = \infty \quad (\text{A.40})$$

Solving (A.40) is not trivial. This is because there is no closed-form solution for Thevenin voltage and thereby there

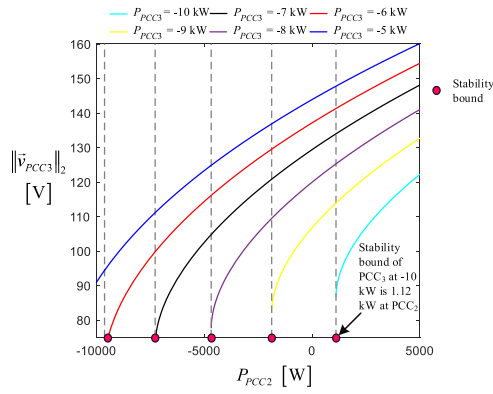


**FIGURE 13.** Stability margin observation from the developed generalized P-V curves at local PCC bus 3 ( $\|\bar{v}_{PCC3}\|_2$ ) (i.e., Morphism 2) showing that after the stability margin the structure of Morphism 2 is not sustained from  $\mathbb{R}^{2N}$  to  $\mathbb{R}$ .

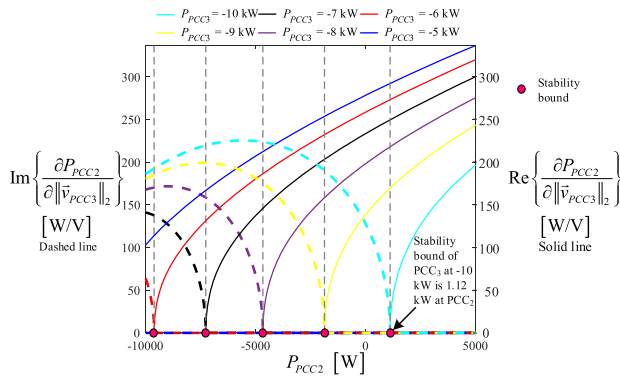


**FIGURE 14.** Stability margin prediction by observing the real and imaginary parts of  $\partial P_{PCC2}/\partial \|\bar{v}_{PCC3}\|_2$ .

is no way to express the derivative of the  $i^{th}$  PCC bus voltage with respect to the  $j^{th}$  PCC bus active power set-point. Nevertheless, for a given network that is shown in Fig. 5 for instance, a derivation concept is provided for the Thevenin voltage expression as function of nearby buses excluding self-set point is provided in the developed morphism 2. The internal PCC buses in Fig. 5 are described by the manifolds (A.41) and (A.42).

$$\|\bar{v}_{PCC2}\|_2 = \frac{\|V_{Th2}\|_2}{2} + \sqrt{\frac{\|V_{Th2}\|_2^2}{4} + R_{Th2}P_{PCC2}}$$

$$\text{where } \|V_{Th2}\|_2 = \left( \sqrt{\frac{\|V_g\|_2^2}{4} + R_{Th3}P_{PCC3}} - \frac{\|V_g\|_2}{2} \right) \times R_{Th2}R_{Th3}^{-1} + \|V_g\|_2 \quad (\text{A.41})$$

$$\|\bar{v}_{PCC3}\|_2 = \frac{\|V_{Th3}\|_2}{2} + \sqrt{\frac{\|V_{Th3}\|_2^2}{4} + R_{Th3}P_{PCC3}}$$

$$\text{where } \|V_{Th3}\|_2 = \sqrt{\frac{\|V_g\|_2^2}{4} + R_{Th2}P_{PCC2}} + \frac{\|V_g\|_2}{2} \quad (\text{A.42})$$

(A.42) is an example of the proposed generalized P-V curve (i.e., Morphism 2) for the internal PCC bus 3 in the network in Fig. 5. Furthermore, this Morphism 2 is plotted in Fig. 13. Specifically, the Morphism 2 structure preservation is not sustained as seen in Fig. 13 after passing the set-point that belongs to the UOR. Moreover, the stability margin can be found in closed-form as in (A.43) for bus 3 with respect to bus 2 of Fig. 5 network.

$$\frac{\partial \|\bar{v}_{PCC3}\|_2}{\partial P_{PCC2}} = \frac{1}{2} \frac{\partial \|V_{Th3}\|_2}{\partial P_{PCC2}} \times \left( 1 + \frac{\|V_{Th3}\|_2}{2\sqrt{\frac{\|V_{Th3}\|_2^2}{4} + R_{Th3}P_{PCC3}}} \right) = \infty$$

$$\text{where } \|V_{Th3}\|_2 = \sqrt{\frac{\|V_g\|_2^2}{4} + R_{Th2}P_{PCC2}} + \frac{\|V_g\|_2}{2},$$

$$\frac{\partial \|V_{Th3}\|_2}{\partial P_{PCC2}} = \frac{R_{Th2}}{2\sqrt{\frac{\|V_g\|_2^2}{4} + R_{Th2}P_{PCC2}}} \quad (\text{A.43})$$

The closed-form solution of (A.43) is expressed in simplified form as (A.44),

$$\frac{\partial \|\bar{v}_{PCC3}\|_2}{\partial P_{PCC2}} = \frac{\Gamma}{\Phi} \quad (\text{A.44})$$

where

$$\Gamma = \frac{R_{Th2}}{4} \times \left( \frac{\left( \frac{\|V_g\|_2}{2} + \sqrt{R_{Th2}P_{PCC2} + \frac{\|V_g\|_2^2}{4}} \right)}{2} \right) \times \left( \frac{\left( \frac{\|V_g\|_2}{2} + \sqrt{R_{Th2}P_{PCC2} + \frac{\|V_g\|_2^2}{4}} \right)^2}{\sqrt{P_{PCC3}R_{Th3} + \frac{\left( \frac{\|V_g\|_2}{2} + \sqrt{R_{Th2}P_{PCC2} + \frac{\|V_g\|_2^2}{4}} \right)^2}} \right) \times \sqrt{P_{PCC3}R_{Th3} + \frac{\left( \frac{\|V_g\|_2}{2} + \sqrt{R_{Th2}P_{PCC2} + \frac{\|V_g\|_2^2}{4}} \right)^2}{4}},$$

$$\Phi = \frac{\|V_g\|_2^2 \sqrt{R_{Th2}P_{PCC2} + \frac{\|V_g\|_2^2}{4}}}{8} + \frac{\|V_g\|_2^3}{16} + \frac{R_{Th2}\|V_g\|_2 P_{PCC2}}{4} + \frac{R_{Th2}P_{PCC2} \sqrt{R_{Th2}P_{PCC2} + \frac{\|V_g\|_2^2}{4}}}{4} + P_{PCC3}R_{Th3} \sqrt{R_{Th2}P_{PCC2} + \frac{\|V_g\|_2^2}{4}}$$

now,  $P_{PCC2}$  value that makes  $\partial P_{PCC2}/\partial \|\bar{v}_{PCC3}\|_2$  equal to zero in (A.44) is the stability margin for bus 3 with respect to active power change at bus 2 of Fig. 5 network. Unfortunately, this involves polynomial with an order higher than 5, finding the deterministic roots of this polynomial is not feasible. This is proved by the fundamental theorem of Galois [28]. Galois theory provides a connection between field theory

and group theory. This connection allows reducing certain problems (i.e., polynomial roots finding for our case) in field theory to group theory such as permutation group of their roots. By Galois theory, it was proven that for a polynomial roots' to be solvable by radicals and the main operations addition, subtraction, division, and multiplications; the order of the polynomial must be less than 5. Alternatively, instead of seeking for  $P_{PCC2}$  that makes the  $\partial P_{PCC2}/\partial \|\vec{v}_{PCC3}\|_2$  equal to zero, the imaginary part of this derivative can be plotted by spanning the active power set-point ( $P_{PCC2}$ ). The stability margin can be predicted by observing a non-zero imaginary part existence. The initial active power set-point where the imaginary value observed in  $\partial P_{PCC2}/\partial \|\vec{v}_{PCC3}\|_2$  is the stability margin. This can be seen in Fig. 14 for the network example Fig. 5. In more details, when  $P_{PCC3} = -7$  kW, the stability margin of PCC bus 3 is  $-7.5$  kW. Meaning that, PCC bus 2 can sink maximumly 7.5 kW before PCC bus 3 reaches to instability. Note that, observing the imaginary part in Fig. 14 shows that after the stability margin the function has a non-zero value but before hitting the stability margin the imaginary part was always zero. This gives an advantage to check whether the set-point will produce an instable voltage situation just by looking at the imaginary part of this derivative. Note that, real-valued functions cannot produce a derivative that has a non-zero imaginary part. In other words, even though these stability margins are deduced from the derivatives of *Morphism 2*, the structural preservation of the *Morphism 2* is not preserved when a non-zero imaginary part is observed at the derivative of these morphisms. Meaning that, the results are valid to provide a conclusion about the structure of *Morphism 2*.

## REFERENCES

- [1] A. Khan, M. Hosseinzadehtaher, M. B. Shadmand, S. Bayhan, and H. Abu-Rub, "On the stability of the power electronics-dominated grid: A new energy paradigm," *IEEE Ind. Electron. Mag.*, vol. 14, no. 4, pp. 65–78, Dec. 2020, doi: [10.1109/MIE.2020.3002523](https://doi.org/10.1109/MIE.2020.3002523).
- [2] N. Xue, X. Wu, S. Gumussoy, and U. Muenz, "Dynamic security optimization for N-1 secure operation of Hawai'i Island system with 100% inverter-based resources," *IEEE Trans. Smart Grid*, vol. 13, no. 5, pp. 4009–4021, Sep. 2022.
- [3] B. Mirafzal and A. Adib, "On grid-interactive smart inverters: Features and advancements," *IEEE Access*, vol. 8, pp. 160526–160536, 2020.
- [4] S. Y. Hadush and L. Meeus, "DSO-TSO cooperation issues and solutions for distribution grid congestion management," *Energy Policy*, vol. 120, pp. 610–621, Sep. 2018.
- [5] T. Zhang, S. Liu, W. Qiu, Z. Lin, and L. Zhu, "KPI-based real-time situational awareness for power systems with high proportion of renewable energy sources," *CSEE J. Power Energy Syst.*, vol. 8, no. 4, pp. 1060–1073, Jul. 2022.
- [6] B. Kroposki, B. Johnson, Y. Zhang, V. Gevorgian, P. Denholm, B.-M. Hodge, and B. Hannegan, "Achieving a 100% renewable grid: Operating electric power systems with extremely high levels of variable renewable energy," *IEEE Power Energy Mag.*, vol. 15, no. 2, pp. 61–73, Mar. 2017.
- [7] Q. Ai, S. Fan, and L. Piao, "Optimal scheduling strategy for virtual power plants based on credibility theory," *Protection Control Mod. Power Syst.*, vol. 1, no. 1, p. 3, Dec. 2016.
- [8] C. Kieny, B. Bersenneff, N. Hadjsaid, Y. Besanger, and J. Maire, "On the concept and the interest of virtual power plant: Some results from the European project fenix," in *Proc. IEEE Power Energy Soc. Gen. Meeting*, Jul. 2009, pp. 1–6, doi: [10.1109/PES.2009.5275526](https://doi.org/10.1109/PES.2009.5275526).
- [9] S. Barrett, "CFCL BlueGen units for virtual power plant project in Netherlands," *Fuel Cells Bull.*, vol. 2012, no. 7, pp. 3–4, 2012.
- [10] A. Y. Fard, M. Easley, G. T. Amariuca, M. B. Shadmand, and H. Abu-Rub, "Cybersecurity analytics using smart inverters in power distribution system: Proactive intrusion detection and corrective control framework," in *Proc. IEEE Int. Symp. Technol. Homeland Secur. (HST)*, Nov. 2019, pp. 1–6, doi: [10.1109/HST47167.2019.9032978](https://doi.org/10.1109/HST47167.2019.9032978).
- [11] Q. Hou, E. Du, N. Zhang, and C. Kang, "Impact of high renewable penetration on the power system operation mode: A data-driven approach," *IEEE Trans. Power Syst.*, vol. 35, no. 1, pp. 731–741, Jan. 2020.
- [12] V. Telukunta, J. Pradhan, A. Agrawal, M. Singh, and S. G. Srivani, "Protection challenges under bulk penetration of renewable energy resources in power systems: A review," *CSEE J. Power Energy Syst.*, vol. 3, no. 4, pp. 365–379, Dec. 2017.
- [13] S. Liu, Z. Lin, Y. Zhao, Y. Liu, Y. Ding, B. Zhang, L. Yang, Q. Wang, and S. E. White, "Robust system separation strategy considering online wide-area coherency identification and uncertainties of renewable energy sources," *IEEE Trans. Power Syst.*, vol. 35, no. 5, pp. 3574–3587, Sep. 2020.
- [14] J. Ye, A. Giani, A. Elasser, S. K. Mazumder, C. Farnell, H. Alan Mantooth, T. Kim, J. Liu, B. Chen, G.-S. Seo, W. Song, M. D. Roig Greidanus, S. Sahoo, F. Blaabjerg, J. Zhang, L. Guo, B. Ahn, M. B. Shadmand, N. R. Gajanur, and M. Ali Abbaszada, "A review of cyber-physical security for photovoltaic systems," *IEEE J. Emerg. Sel. Topics Power Electron.*, vol. 10, no. 4, pp. 4879–4901, Aug. 2022.
- [15] S. Harshbarger, M. Hosseinzadehtaher, B. Natarajan, E. Vasserman, M. Shadmand, and G. Amariuca, "(A Little) ignorance is bliss: The effect of imperfect model information on stealthy attacks in power grids," in *Proc. IEEE Kansas Power Energy Conf. (KPEC)*, Jul. 2020, pp. 1–6, doi: [10.1109/KPEC47870.2020.9167599](https://doi.org/10.1109/KPEC47870.2020.9167599).
- [16] A. Halbouni, T. S. Gunawan, M. H. Habaebi, M. Halbouni, M. Kartiwi, and R. Ahmad, "Machine learning and deep learning approaches for CyberSecurity: A review," *IEEE Access*, vol. 10, pp. 19572–19585, 2022.
- [17] M. R. Endsley and E. S. Connors, "Situation awareness: State of the art," in *Proc. IEEE Power Energy Soc. Gen. Meeting-Converts. Del. Electr. Energy 21st Century*, Jul. 2008, pp. 1–4, doi: [10.1109/PES.2008.4596937](https://doi.org/10.1109/PES.2008.4596937).
- [18] Y. Wang, C. Chen, J. Wang, and R. Baldick, "Research on resilience of power systems under natural disasters—A review," *IEEE Trans. Power Syst.*, vol. 31, no. 2, pp. 1604–1613, Mar. 2016, doi: [10.1109/TPWRS.2015.2429656](https://doi.org/10.1109/TPWRS.2015.2429656).
- [19] X. Cheng, F. C. Huff, and P. Francino, "Optimal load dispatch based on generator reactive capability curve," in *Proc. IEEE Power Eng. Soc. Gen. Meeting*, Jun. 2006, p. 6, doi: [10.1109/PES.2006.1709024](https://doi.org/10.1109/PES.2006.1709024).
- [20] D. Pudjianto, C. Ramsay, and G. Strbac, "Virtual power plant and system integration of distributed energy resources," *IET Renew. Power Gener.*, vol. 1, no. 1, pp. 10–16, Mar. 2007.
- [21] P. Cuffe, P. Smith, and A. Keane, "Capability chart for distributed reactive power resources," *IEEE Trans. Power Syst.*, vol. 29, no. 1, pp. 15–22, Jan. 2014, doi: [10.1109/TPWRS.2013.2279478](https://doi.org/10.1109/TPWRS.2013.2279478).
- [22] A. V. Jayawardena, L. G. Meegahapola, D. A. Robinson, and S. Perera, "Capability chart: A new tool for grid-tied microgrid operation," in *Proc. IEEE PES T&D Conf. Expo.*, Apr. 2014, pp. 1–5, doi: [10.1109/TDC.2014.6863320](https://doi.org/10.1109/TDC.2014.6863320).
- [23] F. L. Müller, J. Szabo, O. Sundstrom, and J. Lygeros, "Aggregation and disaggregation of energetic flexibility from distributed energy resources," *IEEE Trans. Smart Grid*, vol. 10, no. 2, pp. 1205–1214, Mar. 2019, doi: [10.1109/TSG.2017.2761439](https://doi.org/10.1109/TSG.2017.2761439).
- [24] Z. Tan, H. Zhong, Q. Xia, C. Kang, X. S. Wang, and H. Tang, "Estimating the robust P-Q capability of a technical virtual power plant under uncertainties," *IEEE Trans. Power Syst.*, vol. 35, no. 6, pp. 4285–4296, Nov. 2020.
- [25] J. W. Simpson-Porco, "Lossy DC power flow," *IEEE Trans. Power Syst.*, vol. 33, no. 3, pp. 2477–2485, May 2018, doi: [10.1109/TPWRS.2017.2749042](https://doi.org/10.1109/TPWRS.2017.2749042).
- [26] W. J. Tzeng and F. Y. Wu, "Theory of impedance networks: The two-point impedance and LC resonances," *J. Phys. A: Math. Gen.*, vol. 39, no. 27, pp. 8579–8591, Jul. 2006, doi: [10.1088/0305-4470/39/27/002](https://doi.org/10.1088/0305-4470/39/27/002).
- [27] F. Y. Wu, "Theory of resistor networks: The two-point resistance," *J. Phys. A, Math. Gen.*, vol. 37, no. 26, p. 6653, 2004.
- [28] J. Rotman, "The fundamental theorem of Galois theory," in *Galois Theory*, J. Rotman Ed. New York, NY, USA: Springer, 1998, pp. 83–85.



**AHMAD KHAN** (Student Member, IEEE) received the B.Sc. and M.Sc. degrees in electrical engineering from Qatar University, Doha, Qatar, in 2014 and 2017, respectively, and the Ph.D. degree from the Electrical and Computer Engineering Department, Kansas State University, Manhattan, KS, USA, in 2020. He is currently pursuing the Ph.D. degree with the Electrical and Computer Engineering Department, University of Illinois at Chicago, Chicago, IL, USA. He was a Research and Development Intern with Siemens Technology, Princeton, NJ, USA, from June 2021 to January 2022. His research interests include application of advanced control theories to solve issues related to power electronics, power systems, and renewable energy integration. His M.Sc. thesis received the Outstanding Thesis Award at Qatar University, in 2017. He received the Best Paper Award from the IEEE Industrial Electronic Society (IES) in the IEEE 12th International Conference on Compatibility, Power Electronics and Power Engineering (CPE-POWERENG 2018) Conference, in 2018. Also, he received the Best Paper Award in the Second International Conference on Smart Grid and Renewable Energy (SGRE) Conference, in 2019, from IEEE IES. He was a co-recipient of the “IEEE Foundation Industry Application Society (IAS) Myron-Zucker Grant,” in 2019.



**MOHAMMAD B. SHADMAND** (Senior Member, IEEE) received the Ph.D. degree in electrical engineering from Texas A&M University, College Station, TX, USA, in 2015. From 2015 to 2016, he was an Instructor with the Department of Electrical and Computer Engineering, Texas A&M University. From 2016 to 2017, he was a Research Engineer with the Renewable Energy and Advanced Power Electronics Research Laboratory, College Station. From 2017 to 2020, he was an Assistant Professor with the Department of Electrical and Computer Engineering, Kansas State University, Manhattan, KS, USA. Since 2020,

he has been an Assistant Professor with the University of Illinois at Chicago, IL, USA. He has published more than 100 journals and conference papers. His current research interests include distributed self-learning control schemes, advanced model predictive control, grid-following and grid-forming inverters, and intrusion detection system for power electronics dominated grids. He was awarded Michelle Munson Serban Simu Key-stone Research Scholar, Kansas State University, in 2017. He was awarded the 2019 IEEE Myron Zucker Faculty-Student Research Grant. He has awarded multiple best paper awards at different IEEE conferences. He is the General Co-Chair of 50th Annual Conference of the IEEE Industrial Electronics Society (IECON 2024), Chicago, IL. He has served as the Technical Program Co-Chair of the 2019 and 2022 IEEE Smart Grid & Renewable Energy Conference. He serves as an Associate Editor of IEEE TRANSACTIONS ON INDUSTRIAL ELECTRONICS, IEEE TRANSACTIONS ON INDUSTRY APPLICATION, and *IET Renewable Power Generation*.



**SUDIP K. MAZUMDER** (Fellow, IEEE) received the Ph.D. degree in electrical and computer engineering from Virginia Tech, in 2001. He has been a Professor with UIC, since 2001, and as the President of NextWatt LLC, since 2008. He has over 30 years of professional experience and has held research and development and design positions in leading industrial organizations and has worked as a Technical Consultant for several industries. He is a fellow of AAAS, in 2020, and a fellow of IEEE, in 2016, for his contributions related to multi-scale control and analysis of power-electronic systems (PES). He has been the Editor-at-Large of IEEE TPEL, since 2019. He has been a Distinguished Lecturer (DL)/Regional DL for IEEE PELS, since 2016. He has been a PELS AdCom Member and a Member-at-Large, since 2015 and since 2020, respectively. At UIC, he was a recipient of the Distinguished Researcher Award in Natural Sciences and Engineering, in 2020, the Inventor of the Year Award, in 2014, and the University Scholar Award, in 2013. He has received five IEEE awards and NSF career and ONR YIP awards.

...